nature physics



Article

https://doi.org/10.1038/s41567-025-03030-4

Decoding frequency-modulated signals increases information entropy in bacterial second messenger networks

Received: 5 March 2025

Accepted: 12 August 2025

Published online: 15 September 2025



Rongrong Zhang $oldsymbol{0}^{1,2,6}$, Shengjie Wan^{1,2,6}, Jiarui Xiong^{1,3}, Lei Ni^{1,2}, Ye Li $oldsymbol{0}^{1,2}$, Yajia Huang^{1,2}, Bing Li^{1,2}, Mei Li^{1,2}, Shuai Yang $oldsymbol{0}^{4,5} \boxtimes \&$ Fan Jin $oldsymbol{0}^{1,2} \boxtimes$

Bacterial second messenger networks transmit environmental information through both amplitude and frequency modulation strategies. However, the mechanisms by which cells decode frequency-encoded signals remain poorly understood. By reconstructing the cyclic adenosine monophosphate second messenger system in *Pseudomonas aeruginosa*, we demonstrate that frequency-to-amplitude signal conversion emerges through three distinct filtering modules that decode frequency-encoded signals into gene expression patterns. Our mathematical framework predicts a range of frequency filtering regimes controlled by a dimensionless threshold parameter. We validated these using synthetic circuits and an automated experimental platform. Quantitative analysis reveals that under the given parameter conditions, frequency modulation expands the accessible state space more substantially than amplitude modulation alone. The total number of accessible states scales as the square of the number of regulated genes for frequency-enhanced control, compared with the power of 0.8 for amplitude-only control. This results in approximately two additional bits of information entropy in three-gene systems when using frequency-based control. Our findings establish the fundamental principles of frequency-based signal processing in bacterial second messenger networks, revealing how cells exploit temporal dynamics to regulate multiple genes and expand accessible state spaces. This provides insights into both cellular information physics and design principles for synthetic biology.

Information encoding and transmission in physical systems can be achieved through two fundamental mechanisms: amplitude modulation (AM) and frequency modulation (FM)¹. Although the physics of these mechanisms is well understood in classical signal processing, their implementation in molecular networks presents unique challenges that probe fundamental questions about how cells decode and process information. The dichotomy between AM and FM is particularly striking in cellular networks, where evolution has produced sophisticated regulatory systems that utilize both encoding strategies²-5, raising

deep questions about the physical principles governing biological signal decoding.

The physics of cellular information processing emerges from the interplay between nonlinear dynamics and network topology. Although natural systems have evolved to exploit both AM and FM^{6,7}, frequency-based regulation appears as a recurring motif across diverse cellular contexts—from calcium oscillations⁵ to hormone secretion patterns⁸ and transcription factor dynamics⁹⁻¹². The ubiquity of FM suggests that it represents a fundamental physical principle rather

than a specialized adaptation. Despite its prevalence, the mechanisms enabling cells to decode these frequency-encoded signals remain poorly understood.

Second messenger systems, including those based on cyclic AMP (cAMP), represent one of the primary channels through which cells process and transmit fluctuating signals¹³. These molecular intermediaries translate external stimuli into internal cellular responses, often serving as critical nodes in information processing networks. In bacterial systems, cAMP acts as a central regulator that coordinates gene expression in response to environmental changes, making it an ideal candidate for studying frequency-dependent signal processing^{14,15}.

Synthetic biology has achieved remarkable progress in engineering amplitude-modulated gene circuits, from toggle switches to oscillators and logic gates that perform sophisticated computational operations 16-20. However, creating synthetic systems that can effectively decode frequency-modulated signals has proven substantially more challenging. Although pulse-width modulation (PWM) offers one approach for dynamic regulation 21-24, it fundamentally differs from the rich frequency-dependent behaviours observed in natural systems 25-28 in which information is encoded purely in transition frequencies and constant time averages are maintained. This disconnect between natural and engineered systems highlights a critical gap in our understanding of how temporal dynamics are processed in cellular contexts.

Quantitative understanding of frequency-modulated second messenger systems has remained limited due to experimental complexities. The dynamic nature of these signals, combined with the intricate feedback mechanisms inherent to natural cAMP networks ^{13,15}, has complicated efforts to establish clear frequency response relationships. Previous theoretical work has explored specific aspects of biological FM, such as frequency-to-amplitude coordination ²⁹ and energy optimization in oscillatory systems ³⁰. However, a comprehensive physical framework that connects molecular dynamics to frequency-decoding capabilities has remained elusive. Such a framework must bridge multiple scales—from microscopic molecular interactions to macroscopic information flow—as well as accounting for the fundamental constraints of biochemical networks.

To address this challenge, we reconstructed cAMP second messenger networks in Pseudomonas aeruginosa, creating a simplified and controllable signal transduction system by replacing natural cAMP input pathways with light-controlled production and disrupting downstream transcriptional feedback systems. This synthetic approach enabled the precise control and quantification of cAMP dynamics without interference from endogenous regulatory mechanisms. Using this reconstructed circuit, we present a unified theoretical and experimental investigation of how biological systems decode frequency-modulated information. We develop an analytical framework that reveals a phase transition between distinct filtering behaviours in molecular networks, controlled by a dimensionless parameter that emerges from underlying biochemical dynamics. This framework enables quantitative predictions about how cellular systems convert frequency-encoded signals into precise amplitude outputs across different dynamical regimes.

To comprehensively characterize these dynamic circuits, we constructed an automated high-throughput platform for the systematic validation of our theoretical predictions. Our results demonstrate that the successful decoding of frequency-modulated signals enables biological networks to mathematically expand their accessible state space beyond what is achievable through AM alone. Under specific conditions, coordinated frequency and duty cycle control notably increases the total information entropy compared with amplitude-only modulation, with a more favourable scaling as the number of regulated genes increases. In a three-gene regulatory system, this enhancement through joint frequency-to-amplitude control yields approximately two additional bits of information entropy—effectively multiplying the number of distinguishable expression states by nearly four.

Physical principles of frequency-to-amplitude signal conversion in cAMP second messenger networks

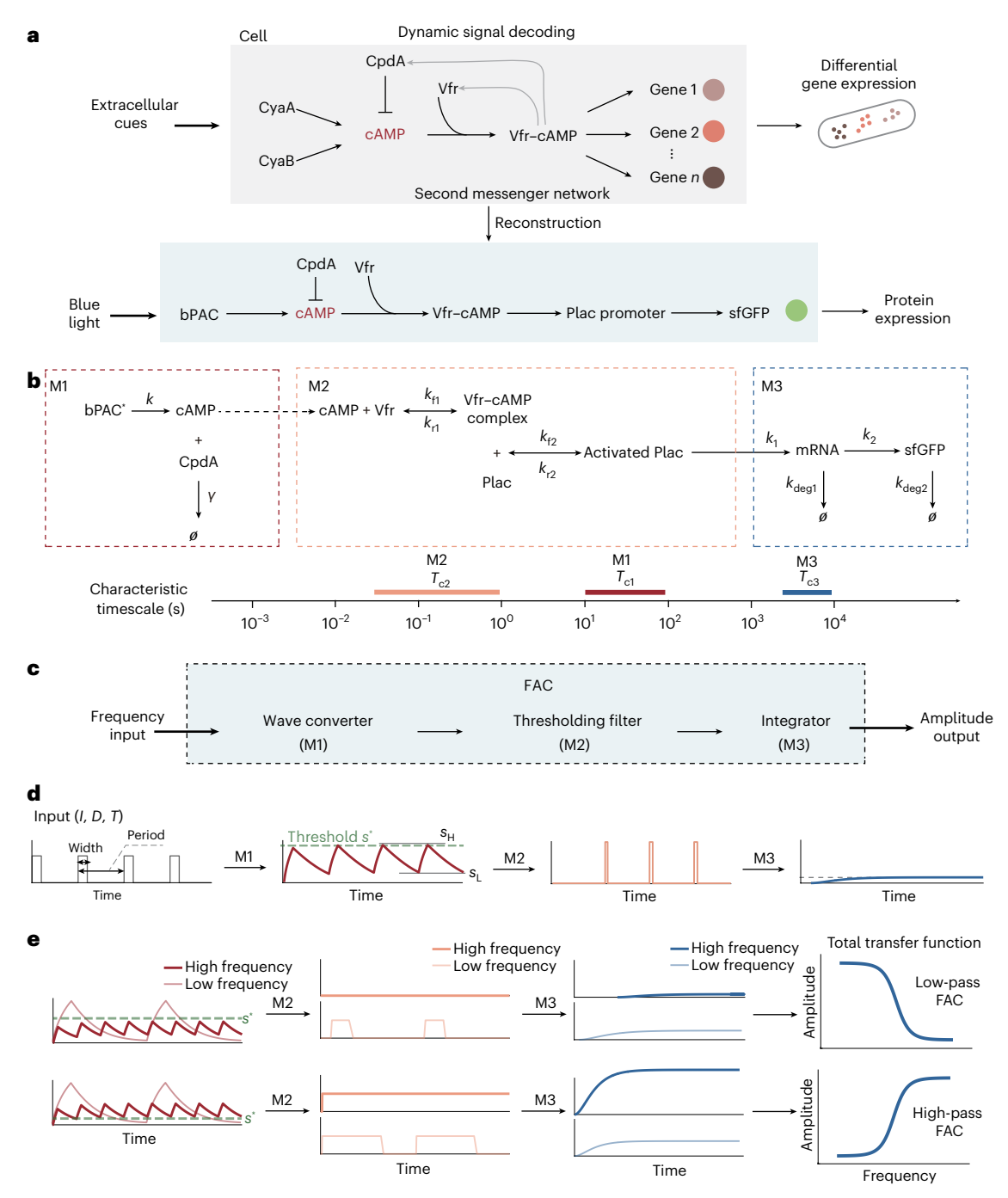
The native cAMP regulatory network in *P. aeruginosa* involves complex signalling mechanisms^{15,31}, including multiple upstream adenylyl cyclases responding to various environmental stimuli, and sophisticated feedback loops through Vfr and CpdA (Fig. 1a, top). This inherent complexity makes isolating and studying frequency-dependent signal processing nearly impossible in natural systems. To overcome this challenge, we reconstructed a streamlined cAMP signalling pathway by replacing endogenous cAMP synthesis machinery with a blue-light-inducible system to precisely simulate environmental perturbations. Additionally, we replaced the native promoters of the cAMP phosphodiesterase CpdA and the effector protein Vfr with constitutive promoters insensitive to cAMP regulation, allowing precise control over their expression levels. By coupling a Vfr–cAMP responsive promoter (Plac) with the *sfGFP* reporter gene, we established a quantitative monitoring system for signal output (Fig. 1a, bottom).

Notably, this reconstructed synthetic signalling system exhibits sophisticated hierarchical signal processing characteristics that naturally emerge from distinct reaction kinetics operating across multiple timescales (Supplementary Note 1). Through rigorous timescale analysis based on established kinetic parameters from the literature, we identified a critical temporal hierarchy within the system that enables sequential information processing (Fig. 1b). The thresholding filter operates at the fastest timescale with characteristic time $T_{c2}(10^{-2}-10^0~{\rm s})$, facilitating rapid Vfr–cAMP binding interactions and promoter activation dynamics 32 . The wave converter functions at an intermediate timescale with characteristic time $T_{c1}(10^0-10^1~{\rm s})$, governed primarily by CpdA-mediated cAMP degradation kinetics 33 . The integrator operates at the slowest timescale with characteristic time $T_{c3}(10^3-10^4~{\rm s})$, determined by the intrinsic rates of protein expression and degradation 34 .

This pronounced temporal separation $(T_{c2} \ll T_{c1} \ll T_{c3})$ is not merely incidental but rather essential for proper circuit function, enabling sequential signal processing and minimizing interference between reaction networks³⁵. The system's distinct timescales naturally partition its functionality into three modules with well-defined transfer functions, collectively forming what we term the frequency-to-amplitude converter (FAC; Fig. 1c). This modular architecture allows us to systematically analyse and predict how frequency-encoded signals are progressively transformed as they propagate through the circuit, providing a physical basis for understanding biological frequency demodulation (Fig. 1d).

The wave converter (M1) functions as a signal transduction module, transforming discrete light inputs into continuous analogue sawtooth patterns of cAMP concentration characterized by a defined peak $(s_{\rm H})$ and trough $(s_{\rm L})$. This transformation occurs through the coordinated action of two opposing processes: the optogenetic control module that regulates cAMP synthesis in response to light stimuli, and the degradation mechanism mediated by CpdA that systematically hydrolyses cAMP. The interplay between these synthesis and degradation kinetics establishes a dynamic equilibrium, generating characteristic concentration oscillations of intracellular cAMP with precisely defined waveforms (Fig. 1b). This module's dynamics are critical for frequency detection, as they encode temporal information into concentration profiles that can be further processed by downstream components.

The thresholding filter (M2) serves as a nonlinear signal processor, converting oscillating cAMP signals through concentration-dependent complex formation with the effector protein Vfr. When Vfr-cAMP complex concentrations exceed specific response thresholds, they activate target promoters, implementing frequency-selective signal processing through cooperative molecular interactions. This molecular filtering mechanism transforms continuous cAMP oscillations into promoter activation events whose temporal pattern depends critically on both input frequency and threshold characteristics.



 $\label{lem:fig.1} Fig. 1 | Reconstruction of cAMP second messenger networks and the hierarchical architecture of frequency-to-amplitude signal conversion.$

 $\label{eq:approx} \textbf{a}, Comparison of cAMP signalling pathways. Top: native complex network in P, $aeruginosa$ with feedback loops. Bottom: streamlined reconstructed pathway with light-inducible cAMP synthesis and constitutive CpdA/Vfr expression for precise control and sfGFP monitoring. \mathbf{b}, Timescale analysis revealing hierarchical signal processing across three temporal domains: thresholding filter (T_{c2}), wave converter (T_{c1}) and integrator (T_{c3}). Temporal separation $(T_{c2} \ll T_{c1} \ll T_{c3})$ enables sequential processing. \mathbf{c}, \mathbf{c} AC architecture integrating a wave converter $(M1)$, thresholding filter $(M2)$ and integrator $(M3)$ modules, each operating P.$

within the characteristic timescales. **d**, Theoretical signal transformation through the FAC system. M1 converts periodic inputs to cAMP sawtooth waveforms, M2 processes oscillations through threshold-dependent activation and M3 integrates filtered signals into stable protein expression. **e**, Filtering characteristics in alternative FAC configurations using idealized threshold filtering. Top: high threshold creates low-pass behaviour. Bottom: low threshold establishes high-pass behaviour. Data in **d** and **e** are generated using ideal threshold approximation; detailed solutions are provided in in Supplementary Notes 2 and 3.

The integrator (M3) acts as the system's memory element, capturing transcriptional activity through protein expression from the activated promoters. This module performs the temporal averaging of the promoter activation events, generating stable protein levels that reflect the time-integrated transcriptional activity. By converting dynamic frequency information into steady-state protein concentrations, this

module completes the frequency-to-amplitude conversion process, providing a stable readout of the original frequency-encoded signals.

Through this sequential processing, the FAC achieves robust frequency-to-amplitude conversion (Fig. 1d). The frequency discrimination capabilities of this architecture emerge from the distinct behaviours of each module, particularly the interaction between the

wave converter's dynamic output and the thresholding filter's activation threshold.

The system's frequency selectivity is primarily determined by the threshold setting (*s*') of the thresholding filter, which emerges from the underlying biochemical properties of Vfr-cAMP interactions. With high threshold settings (Fig. 1e, top), the filter preferentially blocks high-frequency signals and partially transmits low-frequency signals, resulting in a low-pass FAC configuration. Conversely, low-threshold settings (Fig. 1e, bottom) enable the complete transmission of high-frequency signals and attenuate low-frequency signals, thereby establishing a high-pass FAC configuration. This occurs because high-frequency signals consistently exceed the threshold, whereas low-frequency signals fall short or only intermittently cross the threshold (Supplementary Notes 2–4 provide detailed analytical solutions and parameter values).

Our systematic timescale analysis and chemical reaction network (CRN) modelling enabled both temporal signal simulation and comprehensive exploration of dynamic interactions within the circuit (Extended Data Fig. 1 and Supplementary Tables 1–3). This reconstructed architecture, which we name the frequency-decoding cAMP circuit (FDCC), provides a robust platform for implementing and analysing frequency-based gene regulation in second messenger networks and reveals fundamental physical principles governing biological frequency demodulation.

Analytical framework for frequency-to-amplitude signal conversion

Understanding the physical principles of frequency-based information processing in biological networks requires bridging microscopic molecular dynamics with macroscopic system behaviours. To achieve this, we developed two complementary theoretical frameworks. A CRN model (Extended Data Tables 1 and 2 and Supplementary Tables 1–3) captures detailed molecular reaction kinetics³⁶, providing comprehensive simulation capabilities but yielding a parameter space too complex for direct insight extraction. Complementing this, we constructed a dimensionally reduced analytical model that extracts essential system characteristics^{34,37}, revealing the fundamental physics governing the system behaviour. This multilevel approach enables comprehensive analysis from molecular interaction details to system-level properties.

The analytical framework strategically exploits the natural temporal hierarchies within the system, where M2, M1 and M3 operate on millisecond-to-second, second-to-minute and minute-to-hour timescales, respectively. This pronounced temporal separation $(T_{c2} \ll T_{c1} \ll T_{c3})$ enables the modular analysis of each component, leading to analytically tractable equations that reveal how frequency-encoded signals are systematically transformed as they propagate through the circuit. By decomposing the system into functionally distinct modules operating at separate timescales, we can analyse each component independently and capture their coupled interactions through well-defined interfaces. This mathematical approach not only simplifies the analysis but also provides deeper physical insights by isolating the essential mechanisms responsible for frequency discrimination. The resulting analytical framework reveals how specific parameter combinations give rise to distinct high-pass and low-pass filtering behaviours, establishing a quantitative foundation for understanding and engineering biological frequency-to-amplitude conversion systems.

Our modular analysis approach enables the derivation of closed-form expressions that describe the system's steady-state behaviour under periodic stimulation, providing a predictive framework for how frequency-encoded information is processed and transformed into stable gene expression patterns. This analytical tractability stands in contrast to the computational complexity of direct CRN simulations, offering both mechanistic understanding and practical design principles for frequency-responsive biological circuits.

In the M1 module, we established a detailed analysis of the reaction kinetics (Supplementary Note 2) to characterize the system's steady-state behaviour. Under periodic light stimulation, the light-sensitive adenylyl cyclase and phosphodiesterase in M1 regulate the intracellular cAMP concentration through its synthesis (rate k) and hydrolysis (rate γ), respectively. The system achieves a stable oscillatory state, exhibiting a periodic waveform (Fig. 1d). We derived an analytical solution for this dynamic equilibrium within one period, expressed as

$$s(\tau) = \begin{cases} 1 - (1 - s_{L})e^{-\tau}, & 0 \le \tau \le \phi D \\ s_{H}e^{-\tau + \phi D}, & \phi D < \tau \le \phi \end{cases}$$
 (1)

All variables and parameters are presented in the non-dimensionalized form. A comprehensive summary of symbols and abbreviations is provided in Extended Data Tables 1 and 2 and Supplementary Table 4. The duty cycle D represents the fraction of the period during which the light stimulus is active. The non-dimensional concentration $s(\tau)$ represents the relative cAMP level normalized to its theoretical maximum concentration (k/γ) . The time and period are normalized to the characteristic timescale of cAMP hydrolysis (γ^{-1}) , yielding the non-dimensional time $\tau = yt$ and period $\phi = \gamma T$, where γ is the hydrolysis rate of cAMP. Under these steady-state conditions, the non-dimensional maximum and minimum levels of cAMP $(s_{\rm H}$ and $s_{\rm L}$, respectively) are given by

$$s_{\rm H}(\phi, D) = \frac{1 - {\rm e}^{-\phi D}}{1 - {\rm e}^{-\phi}},$$
 (2)

$$s_{\rm L}(\phi, D) = \frac{e^{\phi D} - 1}{e^{\phi} - 1}.$$
 (3)

M2 processes the output signal from M1 through two sequential Hill-type binding interactions: first, the cooperative binding between cAMP and the transcription factor Vfr, characterized by the microscopic dissociation constant K_1 (μ M), and second, the binding of the Vfr–cAMP complex to regulatory promoters, characterized by the microscopic dissociation constant K_2 (μ M). These Hill processes exhibit the fastest dynamics among the three modules, with their characteristic time T_{c2} being substantially shorter than T_{c1} . This pronounced timescale separation allows us to assume that the dynamic response of M2 is effectively instantaneous relative to the cAMP oscillations generated by M1. Consequently, in our theoretical model, the temporal evolution of M2's output depends solely on the time-varying input $s(\tau)$ from M1, with the two Hill processes modulating the signal amplitude (Supplementary Note 3). Following this processing, the fraction of activated promoters $\psi(\tau)$ can be analytically expressed as

$$\psi(\tau) = \frac{\lambda \alpha^2 s(\tau)^2}{1 + (\lambda + 1)\alpha^2 s(\tau)^2}.$$
 (4)

The dimensionless parameter $\lambda = [Vfr]_0/K_2$ denotes the relative abundance of transcription factor Vfr normalized to the microscopic dissociation constant K_2 for Vfr-promoter binding, capturing the impact of transcription factor availability in the system. The parameter $\alpha = (k/\gamma)/K_1$ characterizes the cAMP signal strength, defined as the ratio of maximum achievable cAMP concentration (k/γ) to the microscopic dissociation constant K_1 for Vfr-cAMP binding, reflecting the relative strength of the cAMP signalling pathway.

M3 functions to integrate and average the output from M2, representing the protein expression level from promoters activated by Vfr–cAMP complexes. Assuming negligible basal expression from the regulated promoters, we derived the theoretical relationship between periodic input signals and steady-state protein expression (Supplementary Note 4). In the steady state, the time-averaged protein expression level over one period can be expressed as

$$\bar{y} = \frac{1}{\phi} \int_{0}^{\phi} \psi(\tau) d\tau, \tag{5}$$

where \bar{y} represents the dimensionless protein expression level normalized to its maximum achievable value. Through mathematical analysis of this temporal integration, we obtained an analytical solution for the steady-state expression level:

$$\bar{y}(\alpha, \phi, D, \lambda) = \frac{1}{\phi} \left[\frac{\lambda \alpha^2}{1 + (\lambda + 1)\alpha^2} \ln \left[\frac{\sqrt{1 + (\lambda + 1)\alpha^2 s_H^2}}{\sqrt{1 + (\lambda + 1)\alpha^2 s_L^2}} \right] - \frac{\alpha \lambda / \sqrt{\lambda + 1}}{1 + (\lambda + 1)\alpha^2} \tan^{-1} \left(\frac{\alpha \sqrt{\lambda + 1}(s_H - s_L)}{1 + (\lambda + 1)\alpha^2 s_L s_H} \right) \right] + \frac{\lambda \alpha^2 D}{1 + (\lambda + 1)\alpha^2}$$
(6)

This solution quantitatively describes how the system transforms frequency-encoded inputs into defined protein expression levels through the sequential processing of the three modules.

In the theoretical analysis, we first examined the system behaviour when D equals 1. Under this condition, $s_H = s_L = 1$, and equation (6) reduces to a pure amplitude-dependent expression:

$$y^* = \bar{y}(D=1) = \bar{y}(\alpha, \lambda) = \frac{\lambda \alpha^2}{1 + (\lambda + 1)\alpha^2},\tag{7}$$

where y' represents the FDCC response at full duty cycle, determined by parameters α and λ . The amplitude dependence enters through the parameter $\alpha = k/(\gamma K_1)$, where the effective cAMP synthesis rate $k = k_0$ [bPAC'] is directly controlled by light intensity / through the concentration of photoactivated adenylyl cyclase [bPAC']. Higher light intensities increase [bPAC'], thereby elevating k and α , which directly modulates the output response y'. This simplified case serves as a reference point for understanding the system's basic amplitude response characteristics.

To analyse the frequency-dependent behaviour, we identified a critical threshold in M2's filtering characteristics by examining the inflection point of equation (4) (where $d^2\psi/ds^2 = 0$). This is the point at which the system's response sensitivity is the maximum, as it marks the steepest rate of change in the input–output relationship. This analysis yielded a threshold value s^* for the non-dimensional cAMP concentration: $s^* = 1/\sqrt{3\alpha^2(\lambda+1)}$ (Supplementary Note 5).

This threshold characterizes the filtering properties of M2, representing the concentration at which the rate of change in promoter activation is the maximum. Using this threshold definition, we combined equations (6) and (7) to obtain a comprehensive expression for the system response:

$$\bar{\mathbf{y}}(\alpha, f, D, \lambda) = \mathbf{y}^* (D + G), \tag{8}$$

where

$$G(f, D, s^{*}) = f \left[\ln \left[\sqrt{\frac{1 + (s_{H} / \sqrt{3}s^{*})^{2}}{1 + (s_{L} / \sqrt{3}s^{*})^{2}}} \right] - \sqrt{3}s^{*} \left(\tan^{-1} \left(\frac{\sqrt{3}s^{*}(s_{H} - s_{L})}{(\sqrt{3}s^{*})^{2} + s_{H}s_{L}} \right) \right) \right]$$

$$(9)$$

Here $f = 1/\phi$ represents the non-dimensionalized frequency.

This formulation reveals a sophisticated decomposition of the system's response into three fundamental components (Fig. 2a). First, the AM component y* establishes the baseline response level, which is primarily governed by the system's intrinsic biochemical parameters including the relative abundance of transcription factors (λ) and the strength of cAMP signalling (α). Second, the PWM, represented by D, directly captures the temporal characteristics of the input signal through its duty cycle, reflecting the proportion of time the system

is actively stimulated within each period. Finally, the FM component G introduces a dynamic, frequency-dependent modification to the response, enabling the system to discriminate between signals of different frequencies and maintain the same duty cycle and amplitude. Together, these three components form a comprehensive framework that describes how the FDCC integrates and processes complex temporal signals into defined gene expression patterns.

To facilitate a more intuitive analysis of the system's behaviour, we normalized the output by introducing

$$Y = \frac{\bar{y}}{y^*} = D + G,\tag{10}$$

which represents the total normalized response combining both duty cycle and frequency-dependent effects (Supplementary Note 6). This normalization allows us to examine the frequency response characteristics independently of the amplitude scaling factor y.

To establish a comprehensive macroscopic perspective of the FDCC function, we focused on the difference between high-frequency and low-frequency responses, introducing the metric $Y_{\rm HF}$ – $Y_{\rm LF}$, where $Y_{\rm HF}$ and $Y_{\rm LF}$ represent the normalized outputs at high and low frequencies, respectively. Although the analytical expression for this difference is complex in its general form, we found that it simplifies remarkably in the limiting cases of very high and very low frequencies (Supplementary Note 7). The simplified expression primarily depends on two key parameters: threshold s^* and duty cycle D.

This insight led us to construct phase diagram (Fig. 2b) visualizing $Y_{\rm HF} - Y_{\rm LF}$ as a function of these two critical parameters. The diagram reveals a clear dichotomy in the system's behaviour. As s increases, $Y_{\rm HF} - Y_{\rm LF}$ transitions from positive to negative values, indicating a shift from high-pass to low-pass characteristics. Conversely, increasing D promotes a transition from low-pass to high-pass behaviour. This dual dependence is particularly important because D serves as an experimentally controllable parameter, offering a practical means to modulate the system's frequency response within an appropriate range of s.

Through careful mathematical analysis, we identified a critical boundary between these two regimes, expressed by the relationship $D=3s^{*2}$. This elegant relationship (Fig. 2b (dashed lines) and Supplementary Note 7) provides a clear demarcation between high-pass and low-pass behaviours, offering valuable guidance for circuit design and optimization.

Further quantitative analysis of the Y_{HF} and Y_{LF} metrics revealed fundamental differences between the high-pass and low-pass configurations. High-pass FACs could achieve larger differences in response between high and low frequencies ($|Y_{HF} - Y_{LF}|$) when optimally configured, providing greater potential for frequency discrimination. This enhanced capacity for distinguishing frequency differences makes high-pass configurations particularly attractive for engineering precise frequency-dependent responses. Moreover, we observed a critical limitation in low-pass configurations: for any given s*, low-pass responses generally produced smaller Y values across their operating range. This characteristic poses practical challenges, as smaller output signals are inherently more susceptible to experimental noise and cellular stochasticity, potentially compromising measurement accuracy and reliability (Fig. 2c). Our comprehensive stochastic analysis demonstrates that although intrinsic cellular noise introduces variability in system response, the core frequency discrimination capabilities remain intact(Extended Data Fig. 1), with noise effects primarily dependent on transcriptional components and signal strength relative to the theoretical detection threshold. We analysed how system noise affects the response to high- and low-frequency signal decoding, confirming that high-pass configurations maintain superior noise tolerance compared with low-pass systems (Supplementary Fig. 1 and Supplementary Note 8.1). This inherent limitation of low-pass configurations, combined with their reduced frequency discrimination capability, provided a clear rationale for our experimental strategy. Consequently, we

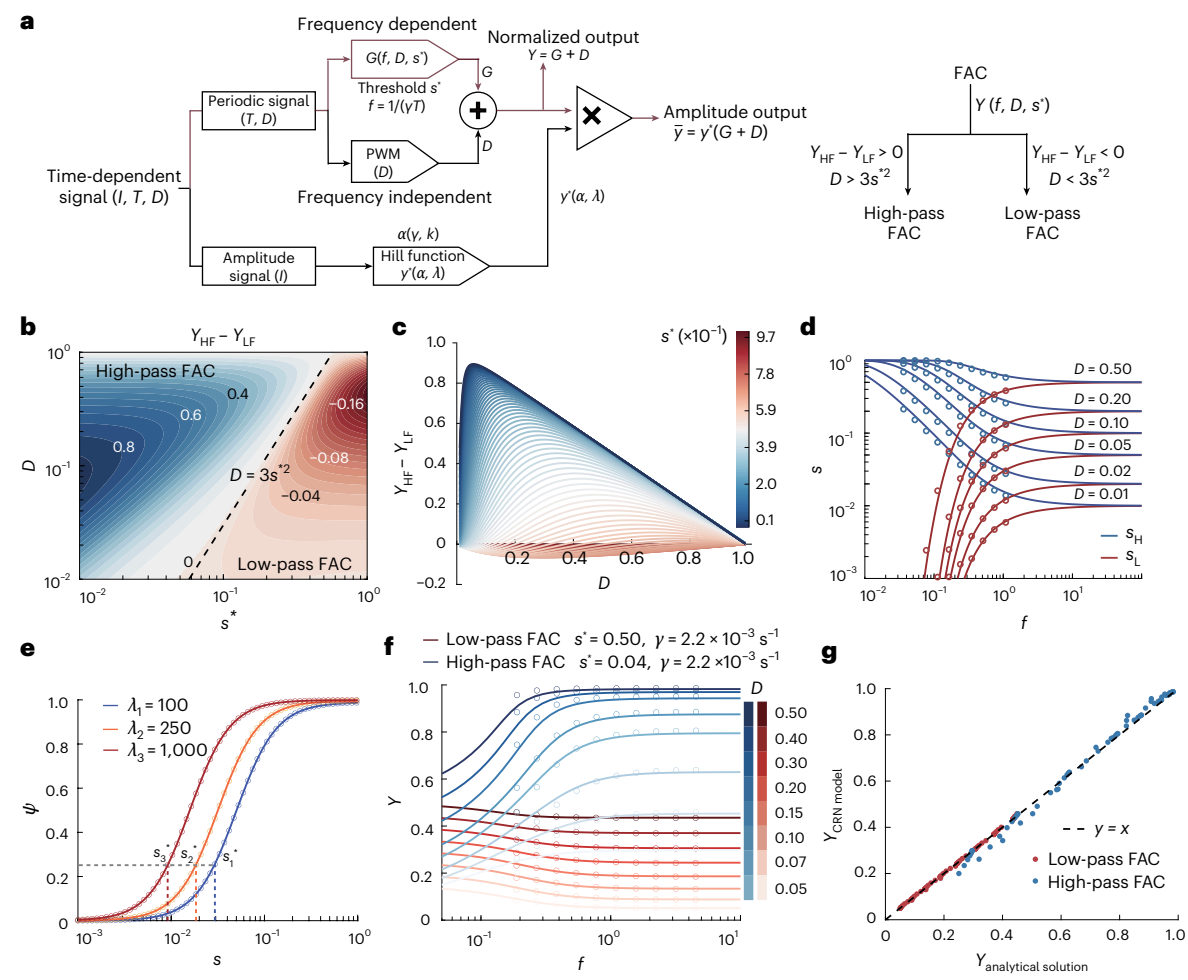


Fig. 2| **Theoretical framework and validation of the FDCC. a**, Decomposition of FDCC response into AM (y'), PWM (D) and FM (G) components. **b**, Phase diagram showing high-pass/low-pass FAC transition. Dashed line ($D = 3s^2$) marks the theoretical boundary. Colour indicates the $Y_{\rm HF} - Y_{\rm LF}$ difference (evaluated at $10^{-1} \, {\rm s}^{-1}$ and $10^{-5} \, {\rm s}^{-1}$). **c**, Frequency discrimination capability versus duty cycle. High-pass FACs show enhanced discrimination compared with low-pass configurations. **d**, Maximum ($s_{\rm H}$) and minimum ($s_{\rm L}$) signal levels versus frequency

and duty cycle. Lines, theory; circles, CRN simulations. **e**, Thresholding filter activation profiles showing analogue processing capabilities modulated by λ . Threshold positions: s_1 = 0.029 (λ_1 = 100), s_2 = 0.018 (λ_1 = 250) and s_3 = 0.009 (λ_1 = 1,000). **f**, Normalized output (Y) for high-pass and low-pass configurations. Lines, theory; points, CRN simulations across different duty cycles. **g**, Theorysimulation correlation across the complete parameter space (R^2 = 0.992), validating the analytical framework accuracy.

prioritized the investigation and implementation of high-pass FACs and conducting more limited studies of low-pass configurations primarily to validate our theoretical framework.

To develop a more comprehensive understanding of the system's behaviour, we expanded our analysis through additional phase diagrams that explored the interplay between s^* , D and the non-dimensionalized frequency f. These diagrams mapped their influences on both frequency response function G and final output $\bar{y}(f,D,s^*)$ (Supplementary Fig. 2). This expanded parameter space exploration not only validated our theoretical predictions but also provided practical insights for optimizing circuit performance across different operating conditions.

The dynamic behaviour of M1 reveals sophisticated signal processing capabilities (Fig. 2d). At constant periods, higher D values lead to increased maximum (s_H) and minimum (s_L) signal levels, demonstrating how the system accumulates the signal during the 'on' phase of each cycle. When the duty cycle is fixed, increasing frequency causes s_H to decrease whereas s_L rises, both asymptotically approaching D. This convergence of signal bounds at high frequencies reflects a fundamental characteristic of the system's temporal signal processing capability.

M2 exhibits sophisticated signal processing behaviour that transcends conventional binary switching mechanisms (Fig. 2e). Although

our initial conceptual framework suggested a sharp threshold (Fig. 1b), the implemented biological system reveals a more nuanced response landscape. Rather than enforcing an abrupt transition at a fixed threshold value, M2 creates a continuous activation profile in which the promoter activity undergoes a gradual transition between inactive and active states. This analogue processing capability emerges from the cooperative binding dynamics between cAMP and the Vfr transcription factor, with the activation threshold manifesting as a responsive range rather than a discrete point (Extended Data Fig. 1). The system's filtering characteristics can be precisely tuned through transcription factor abundance (λ), where higher λ values systematically shift the activation profile towards lower cAMP concentrations. This tunable analogue filtering mechanism not only provides more sophisticated control over frequency response characteristics but also better reflects the inherent complexity of biological signal processing.

The integration of M1 and M2 dynamics produces distinct frequency-dependent behaviours in the circuit output. In the low-pass configuration (Fig. 2f), increasing frequency progressively attenuates the expression level at fixed duty cycles. Conversely, high-pass configurations (Fig. 2f) show enhanced expression at higher frequencies, demonstrating the circuit's ability to selectively respond to different frequency ranges. This frequency selectivity emerges from the

nonlinear interaction between the wave converter's signal processing and the thresholding filter's activation dynamics.

To assess the validity of our timescale separation assumption, we compared normalized output predictions from both CRN simulations and analytical solutions across the entire accessible parameter space (Fig. 2g). The exceptional correlation (R^2 = 0.992) between these independent approaches confirms that our analytical decomposition successfully captures the essential dynamics of the system. This agreement is particularly important because the CRN simulations implement all microscopic molecular interactions without any predetermined hierarchical organization, yet produce results that align precisely with our analytical predictions derived from modular timescale separation. This validation spans multiple orders of magnitude in key parameters, confirming that the simplified analytical model accurately represents the fundamental physics governing frequency-to-amplitude conversion in the complete reaction network.

These results validate our theoretical framework across multiple scales of analysis—from microscopic reaction kinetics to macroscopic system behaviours. By identifying the critical dimensionless parameters and phase boundaries that dictate system behaviour, this framework not only advances our fundamental understanding of biological frequency processing but also provides quantitative design principles for engineering synthetic circuits with programmable frequency response characteristics.

Specifically, our analysis reveals that the dimensionless threshold parameter $s^* = 1/\sqrt{3\alpha^2(1+\lambda)}$ emerges as the critical determinant of filtering behaviour, with its value relative to D establishing whether the system exhibits high-pass ($s^* < \sqrt{D/3}$) or low-pass ($s^* > \sqrt{D/3}$) characteristics. This parameter encapsulates the interplay between λ and α , revealing how molecular concentrations directly shape the frequency response properties.

The mechanistic principle underlying frequency discrimination emerges from the dynamic interaction between time-varying cAMP signals and the nonlinear activation threshold of the Vfr-promoter system. At high frequencies, cAMP oscillates with reduced amplitude but elevated minimum concentrations, allowing systems with low thresholds to maintain persistent activation. Conversely, at low frequencies, cAMP reaches higher peak concentrations but drops to lower minima, favouring systems with high thresholds. This physical mechanism establishes a direct link between molecular kinetics and frequency-dependent gene expression, a principle probably used by several natural second messenger signalling networks.

Automated measurement platform for quantifying frequency-dependent dynamics in cellular signal processing

Our synthetic biology implementation translates the theoretical FAC architecture into a precisely engineered genetic circuit in P. aeruginosa, enabling the precise control of gene expression through both molecular and operational parameters (Extended Data Table 3 and Supplementary Note 9). M1 is realized through the optogenetically controlled adenylyl cyclase bPAC and the phosphodiesterase CpdA, which together regulate intracellular cAMP dynamics. Light intensity directly controls bPAC activation, determining the cAMP synthesis rate k, whereas CpdA expression levels set the degradation rate y. M2 is implemented through the Vfr transcription factor, which forms complexes with cAMP to activate the target promoters. Vfr concentration directly corresponds to the parameter λ in our model, whereas Vfr-cAMP binding affinity corresponds to parameter K_2 . M3 consists of the sfGFP fluorescent reporter under control of the Vfr-responsive promoter, providing a quantitative readout of the circuit's frequency response. At the molecular level, the circuit can be tuned through CpdA and Vfr expression levels, which affect parameters α and λ , whereas at the operational level, it responds to experimental parameters including light intensity (1) and duty cycle (D). These complementary control mechanisms collectively shape the circuit's output (*Y*), providing multiple degrees of freedom for engineering the desired frequency responses. To systematically explore this multidimensional parameter space, we constructed 65 distinct FDCC variants with different combinations of CpdA and Vfr expression levels (Supplementary Notes 10 and 11 and Supplementary Fig. 3).

To address these challenges, we developed a high-throughput automated experimental platform capable of maintaining stable bacterial states through continuous culture (Fig. 3a). The platform integrates four core functional modules: (1) an optoplate for programmable light signal control, (2) bacterial culture agitation, (3) automated solution handling for continuous dilution and (4) fluorescence measurement. This integrated system enables parallel testing of multiple 96 experimental samples and providing independent control of light signal parameters for individual wells (Supplementary Fig. 4). The continuous dilution culture maintains stable growth rates, preventing protein concentration fluctuations from growth phase transitions, whereas automated fluorescence measurements enable systematic data collection.

The automated workflow follows a rigorously controlled process (Fig. 3b). Under constant temperature and agitation conditions, bacterial strains receive independently programmed light signals via the optoplate control unit (OPCU) device. Hourly sampling cycles remove 50 μl for fluorescence measurement, whereas the remaining culture undergoes rapid dilution (4 min) with a fresh medium. This precise temporal control ensures cultivation continuity and minimizes perturbations to bacterial growth states (Supplementary Note 12 and Supplementary Figs. 4 and 5).

Platform validation demonstrated exceptional stability and reproducibility. The system maintained optical density (OD) at 0.09 ± 0.01 across 96 parallel samples over extended periods (>12 h; Fig. 3c). Even with varying initial conditions, continuous dilution established consistent OD values within -4 h. Cross-batch reproducibility analysis revealed excellent consistency in fluorescence measurements, with coefficients of variation below 10% (Fig. 3d).

To systematically characterize the circuit behaviour, we first mapped the relationship between key parameters (γ and s) and frequency response characteristics (Fig. 3e). Parameter estimation for y and s* was performed using two complementary fitting approaches (Supplementary Note 14). Our systematic approach involved engineering 65 distinct FDCC variants by varying promoters and RBS sequences controlling CpdA and Vfr expressions, followed by staged parameter fitting with physiological constraints (Extended Data Fig. 2 and Supplementary Notes 13 and 14). Since y depends on CpdA and Vfr concentrations and λ scales directly with the Vfr concentration, we obtained strains with varying γ , α and λ values (Supplementary Table 5). The resulting phase diagram reveals distinct regions corresponding to different frequency-to-amplitude conversion behaviours, with $Y_{HF} - Y_{LF}$ serving as a metric for frequency discrimination capability. For this metric, Y_{1F} was evaluated at frequencies corresponding to bacterial division cycles (approximately 1/2,400 s⁻¹), ensuring stable cellular states during measurement periods. The high-frequency response (Y_{HF}) was assessed at $1/100 \,\mathrm{s}^{-1}$, establishing an experimentally accessible range that respects cellular physiological constraints. We strategically selected 23 representative strains from our engineered FDCC variants, shown as circular markers in the phase diagram, to systematically sample different regions of the theoretical parameter space. These strains were specifically chosen to validate our theoretical predictions across diverse operating regimes and maintain experimental feasibility within biological constraints.

Comprehensive frequency response characterization using our automated platform revealed remarkable agreement between theoretical predictions and experimental measurements (Supplementary Note 14.4). Figure 3f presents the frequency response curves for all strains at a fixed D = 0.3, demonstrating consistent alignment across diverse parameter combinations and validating our theoretical framework's predictive power. The parameter fitting procedures

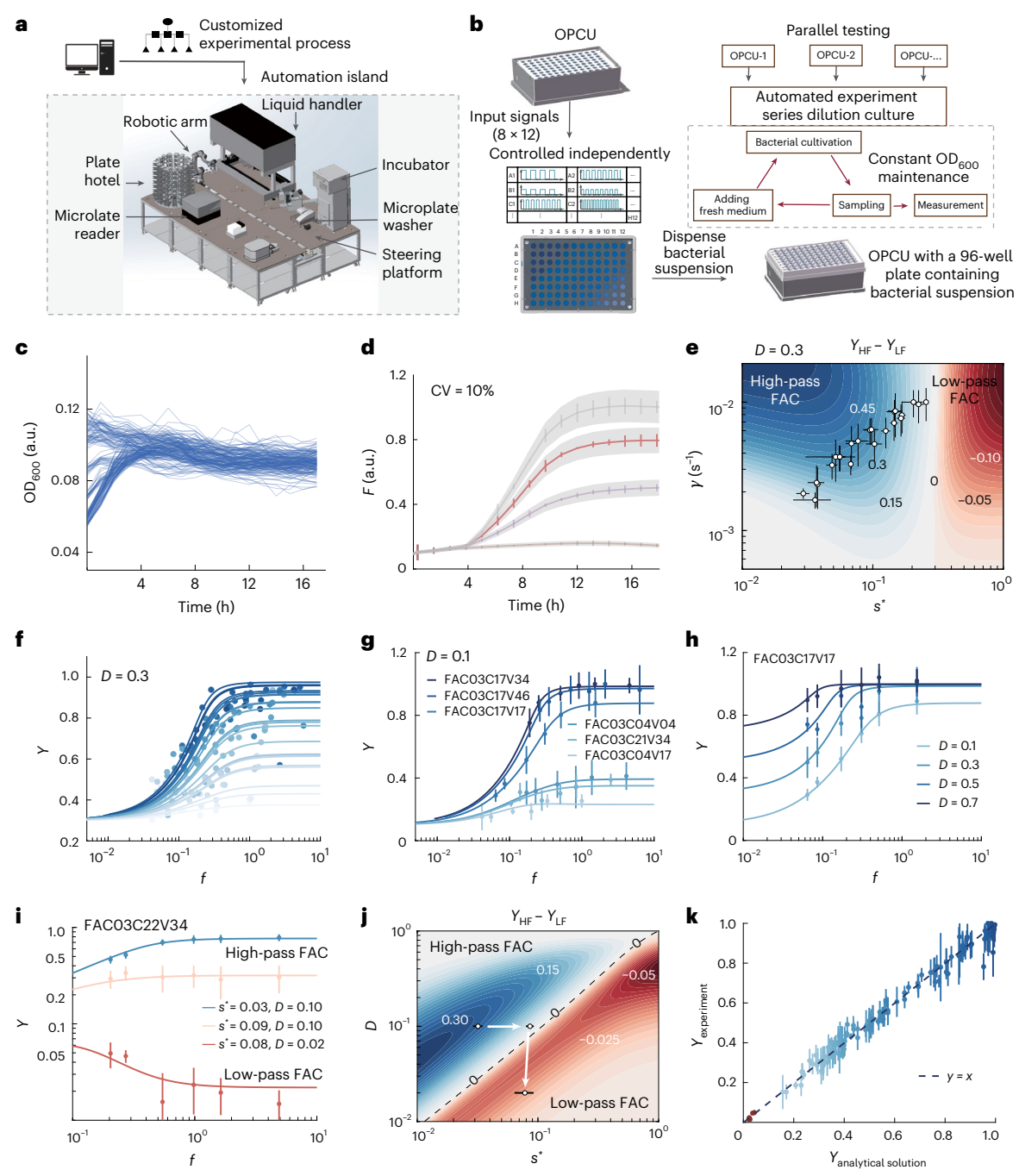


Fig. 3 | **High-throughput automated platform enables the systematic characterization of FDCC frequency responses. a**, Schematic of the automated experimental platform integrating optoplate control, bacterial culture, dilution and fluorescence measurement for the parallel testing of multiple 96 samples. **b**, Workflow: bacterial strains receive programmed light signals via OPCU with hourly cycles of 50-µl sampling and rapid dilution. **c**, Platform stability over >12 h showing OD maintenance at 0.09 ± 0.01 across 96 samples. **d**, Cross-batch reproducibility with <10% variation. Data are presented as mean values; the error bars are standard deviation (s.d.) of the mean; N = 3 independent experiments. CV refers to the coefficient of variation. **e**, Phase diagram of circuit parameters (y, s^*) versus frequency response $(Y_{HF} - Y_{LF})$ at D = 0.3, evaluated at $1/100 \text{ s}^{-1}$ (high frequency) and 1/2, 400 s^{-1} (low frequency). Circular markers, 23 FDCC variants. The error bars are s.d. of the fitted parameters from experimental data

averaged over N=4 independent biological replicates. ${\bf f}$, Frequency response curves at D=0.3. Lines, theory; points, experiments. ${\bf g}$, FDCC variants at D=0.1 showing high-pass behaviours. The error are s.d. of Y mean; N=3 independent biological replicates. ${\bf h}$, Strain FAC03C17V17 across duty cycles. The error bars are s.d. of Y mean; N=4 independent biological replicates. ${\bf i}$, Dynamic switching in FAC03C22V34. The error bars are s.d. of Y mean; N=3 independent biological replicates. ${\bf j}$, Phase diagram mapping of transitions observed in ${\bf i}$, with solid circular points and arrows indicating parameter-driven switches between high-pass and low-pass regimes. Responses are evaluated at $1/100 \, {\bf s}^{-1}$ and $1/2,400 \, {\bf s}^{-1}$. ${\bf k}$, Theory–experiment correlation ($R^2=0.986$). The error bars are s.d. of Y mean; N=3 independent biological replicates. Unless otherwise specified, biological replicates refer to separate cultivation of individual clones.

yielded biologically plausible protein concentrations within the 0.1–5- μ M range, with fitted values showing clear correlation with genetic design choices (Extended Data Tables 1 and 2 and Supplementary Note 14.4).

Our theoretical analysis (Fig. 2b) identified D as a crucial parameter in modulating frequency responses. We validated this prediction through two complementary experimental approaches. First, we characterized several FDCC variants at D=0.1 (Fig. 3g), demonstrating that

circuits maintain their frequency discrimination capabilities even at low duty cycles and exhibiting systematic variations in response to amplitude and frequency sensitivities based on molecular parameters. Second, detailed characterization of a representative strain (FAC03C17V17) across multiple duty cycles (Fig. 3h) revealed how duty cycle modulation systematically alters both response magnitude and frequency sensitivity and maintains fundamental high-pass characteristics. Cross-validation using parameters fitted from the D=0.1 condition successfully predicted responses at other duty cycles without additional parameter adjustment, demonstrating the model's predictive validity.

A particularly crucial finding emerged from the strain FAC03C22V34, which demonstrated controlled switching between high-pass and low-pass FAC behaviours through the precise manipulation of light intensity and duty cycle (Fig. 3i). Light intensity provides direct experimental control over the threshold parameter s through the modulation of the activated bPAC concentration, where higher light intensity increases [bPAC'], thereby raising α and consequently lowering s according to s $\sim 1/\alpha$ (Extended Data Table 3). This dynamic control over the frequency response characteristics revealed the circuit's programmable nature. By mapping these behavioural transitions onto the theoretical phase diagram (Fig. 3j), where solid circular points and connecting arrows track parameter-driven changes, we provided direct experimental validation of the predicted phase boundaries between distinct operating modes.

To assess the validity of our theoretical framework, we compared experimental measurements with theoretical outputs (Y) derived from fitting our mathematical model to each individual experimental condition across the entire accessible parameter space (Fig. 3k). Each data point represents a different combination of strain, frequency, duty cycle and light intensity, where theoretical outputs were calculated using parameters fitted to that specific condition. The exceptional correlation (R^2 = 0.986) between experimental measurements and fitted theoretical outputs spans multiple orders of magnitude in key parameters, demonstrating that our mathematical framework accurately captures the system behaviour across diverse strains and operational conditions.

These detailed characterizations demonstrate that the FDCC architecture implements a well-defined physical system for frequency-dependent information processing in living cells. The quantitative correspondence between theory and experiment across diverse conditions establishes both feasibility and fundamental limits of biological frequency demodulation and provides precise design principles for engineering gene regulatory systems with programmable frequency response characteristics. This physics-based approach to cellular frequency demodulation opens new possibilities for implementing sophisticated computational functions in synthetic biological systems.

Information entropy enhancement through FM

Second messenger systems like cAMP networks naturally coordinate the expression of multiple downstream genes^{15,38,39}, functioning as information processing hubs that translate environmental signals into coordinated cellular responses. After establishing the physical principles governing frequency-to-amplitude conversion in individual circuits, we sought to explore the fundamental mechanisms by which FM could enhance information transmission across biological signal-ling networks.

In biological systems, second messengers typically regulate multiple target genes with diverse response thresholds. FM introduces an orthogonal encoding dimension that potentially expands the accessible state space beyond traditional amplitude-based control. We hypothesized that when multiple genes respond to a single second messenger signal with differing sensitivities, frequency-based control could unlock new regulatory possibilities by accessing regions of state space fundamentally inaccessible through AM alone.

To quantitatively test this hypothesis, we analysed a two-component system in which genes exhibit distinct sensitivities to Vfr-cAMP regulation. These differences are characterized by dissociation constants K_{2A} and K_{2B} , along with their corresponding dimensionless parameters λ_A and λ_B (equation (6)). Here λ_A and λ_B represent the relative abundances of the transcription complexes associated with promoters A and B, respectively. This configuration creates a two-dimensional state space (Y_A, Y_B) with normalized protein expression levels (equation (10)). Although conventional control relies on I and I0, our FDCC architecture introduces I1 as an additional control dimension, enabling the exploration of how information entropy scales with increasing degrees of freedom (Fig. 4a).

To quantitatively analyse state-space accessibility, we introduced a discretization parameter $\epsilon = 0.1$, which functions as a measure of resolution in state-space partitioning. Similar to how the minimum number of spheres N(R) needed to cover a point set scales inversely with sphere radius R as $N(R) \approx 1/R^d$ (ref. 40), the total number of theoretically distinguishable states scales inversely with our discretization parameter ϵ . This parameter divides each dimension of normalized expression (Y) into $1/\epsilon$ equal intervals. In a two-promoter system, our choice of ϵ creates a 10 × 10 grid with 100 theoretically possible distinct expression states (Fig. 4b). Although this discretization provides a simplified metric for quantifying state-space expansion, it is important to note that the actual resolution of distinguishable gene expression states is fundamentally limited by intrinsic cellular noise (Extended Data Fig. 3a and Supplementary Note 15.4). Our choice of ϵ = 0.1 is biologically justified by stochastic analysis, showing that reliable state discrimination requires the separation of at least twice the signal standard deviation (~0.08-0.09), with scaling relationships remaining robust across different ϵ values (Extended Data Fig. 3b and Supplementary Note 15.5). These quantitative noise studies validate our discretization approach and confirm that the observed scaling relationships reflect genuine biological capabilities rather than computational artefacts. Therefore, this grid-based quantification provides a well-grounded measure to demonstrate relative changes in state-space accessibility^{34,41}.

To rigorously quantify the information content of accessible states, we applied Shannon's information theory framework⁴². Assuming a uniform probability distribution across accessible states (which maximizes entropy for a given number of states), we calculated the information entropy $H = -\sum p_i \log_2[p_i]$, where p_i represents the probability of the system occupying state p_i . Under pure AM, we observed only 19 distinct states, represented by the blue curve and corresponding grid cells in Fig. 4b, show an information entropy of $H_{\rm AM} \approx 4.25$ bits. However, introducing FM revealed a remarkable expansion of accessible states. By simultaneously tuning both D and f as frequency was varied from 1 to 1×10^{-3} (non-dimensionalized units), the system accessed additional regions of state space (red grid cells), expanding the total accessible state space to 38 distinct states and increasing the information entropy to $H_{\rm FM} \approx 5.25$ bits.

Our analysis revealed that the accessible state space expands nonlinearly with the increasing number of regulated genes (Extended Data Fig. 3b and Supplementary Note 15.3). In three-gene systems, maintaining the same discretization parameter and exploring the expanded state space (Y_A , Y_B , Y_C), we observed an increase from $H_{AM_3} = \log_2[27] \approx 4.75$ bits under amplitude-only modulation to $H_{FM_3} = \log_2[95] \approx 6.57$ bits when FM is introduced as an additional control dimension, representing a gain of approximately 1.82 bits (Fig. 4c). This higher-dimensional analysis revealed a critical insight: amplitude-only control and combined frequency-to-amplitude control exhibit fundamentally different scaling behaviours as the number of regulated genes increases.

Under the specific diverse response thresholds of multiple target genes, a mathematical analysis of these scaling relationships demonstrated that information entropy under AM scales as $H_{\rm AM} \propto 0.8 \log_2[n]$,

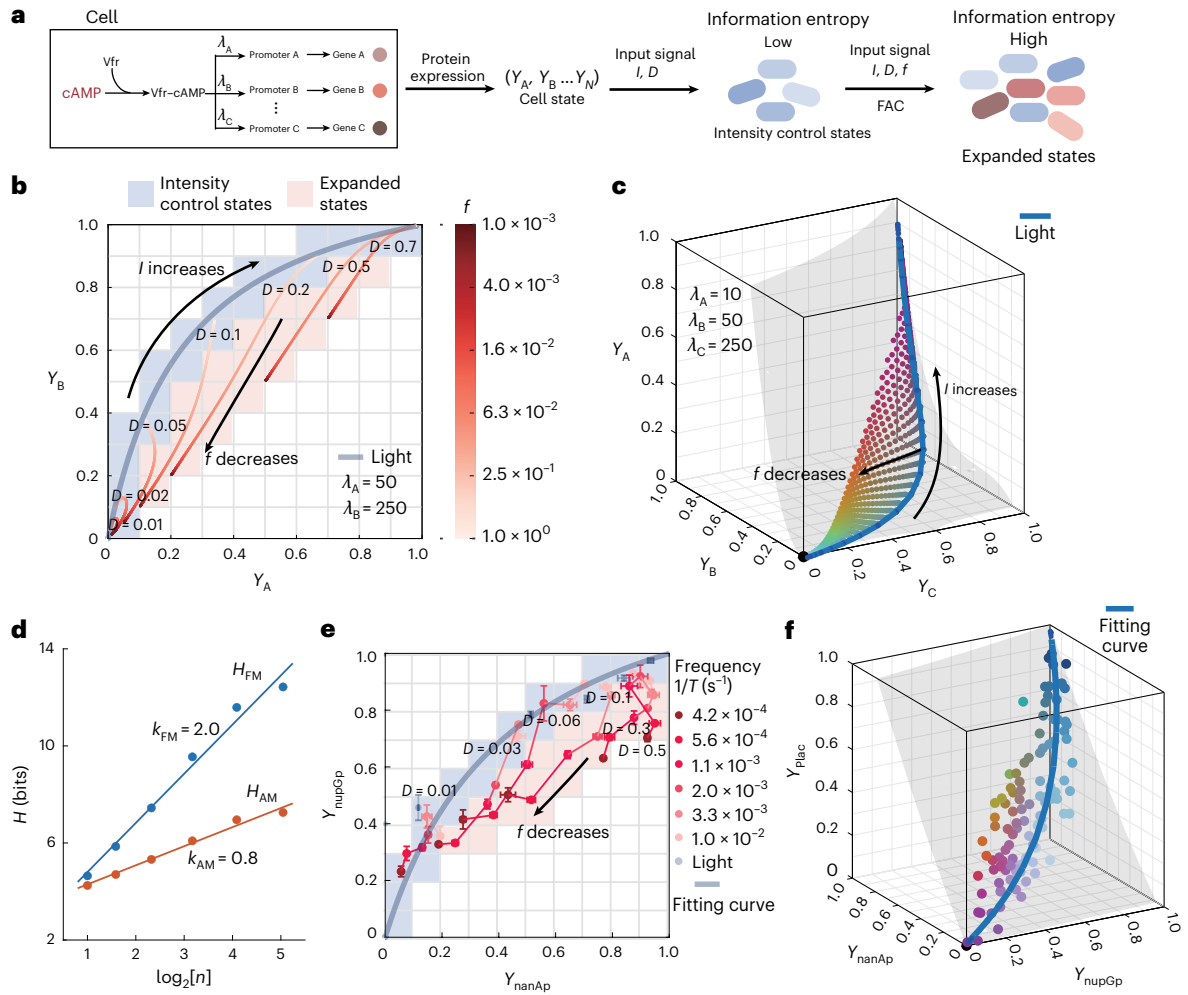


Fig. 4 | **FM increases the information entropy of multigene regulatory systems. a**, Schematic showing frequency control as an additional parameter increasing information entropy beyond AM alone. **b**, Theoretical two-promoter system (ϵ = 0.1 discretization). Blue, amplitude-only states (19 states, ~4.25 bits); red, additional frequency-modulated states. Total, 38 states (-5.25 bits) combining AM and FM. **c**, Three-dimensional state-space expansion from 27 states (-4.75 bits) under AM to 95 states (-6.57 bits) with frequency control. Colour gradient, amplitude only (blue) to frequency modulated

(red). **d**, Information entropy scaling: FM $(H_{\text{FM}} \approx 2.0 \log_2[n])$ (blue) versus AM $(H_{\text{AM}} \approx 0.8 \log_2[n])$ (red) with number of genes n. **e**, Two-promoter experimental validation. Normalized expression (Y) from sfGFP and CyOFP measurements demonstrating entropy expansion. The error bars are s.d. of Y mean for promoters nanAp and nupGp; N=4 independent biological replicates. Colour scheme matches the theoretical predictions in **b**. **f**, Three-promoter system validation using sfGFP, CyOFP and mScarlet measurements, confirming the theoretical predictions shown in **c**.

where n represents the number of regulated genes. By contrast, when FM is introduced as an additional control dimension, it enables a more rapid information entropy scaling of $H_{\rm FM} \simeq 2.0 \log_2[n]$ (Fig. 4d), where $H_{\rm FM}$ represents the total accessible state space achieved through coordinated regulation of α , D and f. This differential scaling reveals that FM's information advantage becomes increasingly pronounced with larger gene networks, as the coordinated temporal dynamics expand the regulatory capabilities beyond what amplitude control alone can achieve. However, this enhancement will ultimately be bounded by physical transmission limits inherent to cellular systems, including molecular noise floors, finite protein concentrations and the temporal resolution of cellular machinery.

To experimentally validate these theoretical predictions, we conducted a high-throughput screening of 260 promoter candidates to identify sets with appropriate λ values (Supplementary Fig. 6 and Supplementary Notes 16 and 17). We constructed both two-gene systems expressing sfGFP and CyOFP (Fig. 4e) and three-gene systems expressing sfGFP, CyOFP and mScarlet (Fig. 4f). Using the same colour mapping scheme as in our theoretical analysis, the experimental results demonstrated clear state-space expansion

through FM in both two- and three-dimensional cases, confirming our theoretical predictions.

These findings provide fundamental insights into both natural and synthetic biological systems. In natural second messenger networks, the more favourable scaling of frequency-based information transmission may explain the prevalence of oscillatory signalling observed across diverse cellular contexts. For synthetic biology, these quantitative scaling laws establish design principles for engineering sophisticated circuit architectures that exploit FM to achieve enhanced control over multiple coordinated outputs. The demonstrated expansion in information entropy represents a physically efficient strategy for increasing the computational capabilities of cellular systems. Our analysis also reveals fundamental frequency resolution limits of the FAC system, including maximum resolvable frequencies (0.025 s⁻¹) determined by cAMP degradation kinetics and minimum distinguishable frequency differences (25% relative change) in the most sensitive operational regions. These resolution characteristics align well with biologically relevant timescales, enabling discrimination between rapid stress responses and sustained metabolic adaptations as well as operating within biophysical constraints (Supplementary Note 8.2).

Summary and perspective

In living systems, information processing extends far beyond simple ON/OFF switching to encompass rich temporal dynamics. Our work reveals a fundamental physical mechanism through which bacterial networks decode frequency-modulated information via a three-module FAC architecture. This system-comprising wave converter, thresholding filter and integrator modules with distinct timescale hierarchies—transforms oscillatory cAMP signals into precise gene expression patterns. By developing FDCCs with programmable frequency responses, we establish a rigorous theoretical and experimental framework that bridges microscopic molecular dynamics with macroscopic information processing. Our analytical model, validated through systematic experimentation on an automated high-throughput platform, reveals that introducing FM as an additional control dimension enables information entropy to scale as $H_{EM} \propto 2.0 \log_2[n]$ compared with amplitude-only control's $H_{AM} \propto 0.8 \log_2[n]$, where n represents the number of regulated genes. This differential scaling provides approximately two additional bits of information in three-gene systems, offering a physical explanation for the prevalence of oscillatory signalling across biological contexts and establishing design principles for engineering sophisticated synthetic circuits with enhanced computational capabilities.

Our information-theoretic approach complements established signal transmission studies that focus on distinguishing input concentrations under noise constraints, typically achieving limited information transmission through individual pathways⁴³. Rather than improving signal discrimination, FM expands regulatory capabilities by enabling the orchestration of complex, coordinated responses across multiple target genes through orthogonal temporal control dimensions. Although our noise analysis (Extended Data Fig. 1 and Supplementary Notes 8 and 15) confirms that intrinsic cellular fluctuations establish fundamental resolution limits, the enhanced entropy scaling reflects genuine capacity for sophisticated pattern generation that extends beyond conventional amplitude-based regulation.

The emergence of dynamic signal processing in gene circuit design marks an important advancement in cellular information processing³. The field of synthetic biology has evolved from constructing basic regulatory elements to developing complex circuits including toggle switch¹⁶, oscillators^{17,18} and logic gates^{19,20}, primarily relying on amplitude-based regulation^{44,45}. However, this amplitude-focused approach captures only part of the rich dynamics observed in natural systems. Recent efforts to incorporate temporal control have led to the development of PWM^{22,23,46}, where information is encoded through variations in signal duration. Although PWM represents progress towards dynamic control, it ultimately remains an extension of amplitude-based regulation, as it relies on modulating time-averaged signal intensity. By contrast, pure FM, where duty cycle remains constant, establishes an independent dimension for information encoding⁴⁷. This fundamental distinction between PWM and FM highlights the untapped potential of frequency-based control in expanding the capabilities of synthetic gene circuits.

Our approach integrates control theory principles with synthetic biology to create a robust theoretical framework. The FAC architecture demonstrates how biological systems can transform frequency-encoded signals into amplitude-modulated gene expression patterns, analogous to engineered FM systems. This framework, combining CRN³⁶ simulations with theoretical analysis³⁴, provides a multiscale understanding from molecular interactions to system-level behaviours. The successful experimental validation through our automated platform demonstrates the feasibility of implementing sophisticated control strategies in living cells.

The development of our automated experimental platform represents a pivotal advancement in synthetic biology's design-build-test-learn cycle⁴⁸. Traditional characterization methods have been insufficient for studying frequency-dependent responses, as they lack

the precision and throughput needed for the systematic analysis of dynamic behaviours⁴⁹⁻⁵¹. Our platform addresses these limitations by enabling the parallel testing of multiple strains and maintaining precise control over both cellular states and dynamic inputs. This technical advance, combined with recent developments in automated screening systems⁴⁹, establishes a new experimental paradigm for studying frequency-modulated gene circuits. The integration of theory and automated experimentation not only validates our theoretical predictions but also provides a generalizable approach for investigating complex dynamic behaviours in biological systems.

Our experimental findings, coupled with observations from natural systems, provide compelling evidence for the significance of frequency-modulated signal processing in cellular information processing. We demonstrated that FM increases the information entropy of signalling pathways by enabling the global regulation of multiple target genes with different activation thresholds or affinities. This was particularly evident in our multigene system experiments, where FM notably increased the information entropy of gene expression patterns, achieving up to two bits of additional information content in three-gene systems. This increased information processing capability mirrors natural systems, where FM facilitates the proportional co-regulation of diverse target genes, as observed in the pulsatile behaviour of transcription factors such as p53 (ref. 52), Ascl1 (ref. 53), NF-kB (ref. 54), Msn2 (ref. 10) and the SOS stress response system¹². Notably, FM provides a mechanism linking individual protein dynamics to large regulon expression, suggesting its role in orchestrating genome-scale expression patterns. Given its observed functions in protein and metabolic networks, as well as transcriptional regulation, we anticipate that frequency-modulated regulation may represent a general principle by which cells encode, process and respond to dynamic environmental signals with expanded information content.

From a synthetic biology perspective, frequency-modulated circuits offer distinct advantages through their relatively simple genetic architecture 55. The FAC system requires a modest set of genetic elements compared with traditional synthetic circuits that often demand multiple regulatory components and precise expression balancing. This architectural simplicity, combined with sophisticated control capabilities, suggests that integrating frequency-modulated regulation into synthetic circuits is not only feasible but potentially transformative. Moreover, incorporating dynamic frequency-based control into engineered circuits presents unique opportunities to effectively address and exploit inherent cellular characteristics, such as noise management and shared regulatory resource allocation 56. This approach to circuit design opens new possibilities for engineering cellular behaviours in ways previously unexplored in traditional engineering disciplines.

Looking forward, this understanding of frequency-based signal processing opens new avenues in both fundamental research and practical applications. In metabolic engineering, the coordination of multiple genes through FM could enable sophisticated pathway control. The expanded state space accessible through FM provides new tools for fine tuning cellular behaviour and controlling complex phenotypes. Furthermore, the connection between single-protein dynamics and genome-wide expression patterns may offer insights into coordinated cellular responses across different organizational scales, potentially revealing new principles for both synthetic biology design and natural regulatory networks.

Several important challenges and opportunities remain for future research. These include developing more sophisticated frequency-responsive elements, improving methods for temporal control of cellular systems and better understanding of noise characteristics in frequency-modulated circuits. Additionally, exploring FM in diverse cellular contexts and organisms could reveal new applications and design principles, further expanding the potential of this regulatory approach in synthetic biology.

Online content

Any methods, additional references, Nature Portfolio reporting summaries, source data, extended data, supplementary information, acknowledgements, peer review information; details of author contributions and competing interests; and statements of data and code availability are available at https://doi.org/10.1038/s41567-025-03030-4.

References

- Roder, H. Amplitude, phase, and frequency modulation. Proc. Inst. Radio Eng. 19, 2145–2176 (1931).
- Hao, N. & O'shea, E. K. Signal-dependent dynamics of transcription factor translocation controls gene expression. *Nat. Struct. Mol. Biol.* 19, 31–39 (2012).
- Purvis, J. E. & Lahav, G. Encoding and decoding cellular information through signaling dynamics. Cell 152, 945–956 (2013).
- 4. Li, P. & Elowitz, M. B. Communication codes in developmental signaling pathways. *Development* **146**, 170977 (2019).
- Cai, L., Dalal, C. K. & Elowitz, M. B. Frequency-modulated nuclear localization bursts coordinate gene regulation. *Nature* 455, 485–490 (2008).
- Micali, G., Aquino, G., Richards, D. M. & Endres, R. G. Accurate encoding and decoding by single cells: amplitude versus frequency modulation. *PLoS Comput. Biol.* 11, e1004222 (2015).
- Szischik, C. L., Reves Szemere, J., Balderrama, R., Vega, C. & Ventura, A. C. Transient frequency preference responses in cell signaling systems. npj Syst. Biol. Appl. 10, 86 (2024).
- 8. Brabant, G., Prank, K. & Schofl, C. Pulsatile patterns in hormone secretion. *Trends Endocrinol. Metab.* **3**, 183–190 (1992).
- Li, C., Cesbron, F., Oehler, M., Brunner, M. & Höfer, T. Frequency modulation of transcriptional bursting enables sensitive and rapid gene regulation. Cell Syst. 6, 409–423 (2018).
- Hansen, A. S. & O'Shea, E. K. Limits on information transduction through amplitude and frequency regulation of transcription factor activity. *eLife* 4, e06559 (2015).
- Behar, M. & Hoffmann, A. Understanding the temporal codes of intra-cellular signals. Curr. Opin. Genet. Dev. 20, 684–693 (2010).
- Locke, J. C., Young, J. W., Fontes, M., Jiménez, M. J. H. & Elowitz, M. B. Stochastic pulse regulation in bacterial stress response. Science 334, 366–369 (2011).
- 13. Gomelsky, M. cAMP, c-di-GMP, c-di-AMP and now cGMP: bacteria use them all. *Mol. Microbiol.* **79**, 562–565 (2011).
- 14. Newton, A. C., Bootman, M. D. & Scott, J. D. Second messengers. Cold Spring Harb. Perspect. Biol. 8, 005926 (2016).
- McDonough, K. A. & Rodriguez, A. The myriad roles of cyclic AMP in microbial pathogens: from signal to sword. *Nat. Rev. Microbiol.* 10, 27–38 (2012).
- Gardner, T. S., Cantor, C. R. & Collins, J. J. Construction of a genetic toggle switch in *Escherichia coli*. *Nature* 403, 339–342 (2000).
- Stricker, J. et al. A fast, robust and tunable synthetic gene oscillator. Nature 456, 516–519 (2008).
- Elowitz, M. B. & Leibler, S. A synthetic oscillatory network of transcriptional regulators. *Nature* 403, 335–338 (2000).
- Jones, T. S., Oliveira, S. M., Myers, C. J., Voigt, C. A. & Densmore, D. Genetic circuit design automation with Cello 2.0. Nat. Protoc. 17, 1097–1113 (2022).
- Moon, T. S., Lou, C., Tamsir, A., Stanton, B. C. & Voigt, C. A. Genetic programs constructed from layered logic gates in single cells. *Nature* 491, 249–253 (2012).
- Davidson, E. A., Basu, A. S. & Bayer, T. S. Programming microbes using pulse width modulation of optical signals. *J. Mol. Biol.* 425, 4161–4166 (2013).

- Benzinger, D. & Khammash, M. Pulsatile inputs achieve tunable attenuation of gene expression variability and graded multi-gene regulation. *Nat. Commun.* 9, 3521 (2018).
- 23. Benzinger, D., Ovinnikov, S. & Khammash, M. Synthetic gene networks recapitulate dynamic signal decoding and differential gene expression. *Cell Syst.* **13**, 353–364 (2022).
- Ravindran, P. T., McFann, S., Thornton, R. H. & Toettcher, J. E. A synthetic gene circuit for imaging-free detection of signaling pulses. *Cell Syst.* 13, 131–142 (2022).
- 25. Bettenworth, V. et al. Frequency modulation of a bacterial quorum sensing response. *Nat. Commun.* **13**, 2772 (2022).
- Albeck, J. G., Mills, G. B. & Brugge, J. S. Frequency-modulated pulses of ERK activity transmit quantitative proliferation signals. *Mol. Cell* 49, 249–261 (2013).
- Paszek, P., Jackson, D. A. & White, M. R. Oscillatory control of signalling molecules. *Curr. Opin. Genet. Dev.* 20, 670–676 (2010).
- 28. Berridge, M. J. The AM and FM of calcium signalling. *Nature* **386**, 759–760 (1997).
- Zhong, Z., Lin, W. & Qin, B.-W. Modulating biological rhythms: a noncomputational strategy harnessing nonlinearity and decoupling frequency and amplitude. *Phys. Rev. Lett.* 131, 138401 (2023)
- Qin, B.-W., Zhao, L. & Lin, W. A frequency-amplitude coordinator and its optimal energy consumption for biological oscillators. Nat. Commun. 12, 5894 (2021).
- Fuchs, E. et al. In vitro and in vivo characterization of the Pseudomonas aeruginosa cyclic AMP (cAMP) phosphodiesterase CpdA, required for cAMP homeostasis and virulence factor regulation J. Bacteriol. 192, 2779–2790 (2010).
- 32. Mazzocca, M., Colombo, E., Callegari, A. & Mazza, D. Transcription factor binding kinetics and transcriptional bursting: what do we really know? *Curr. Opin. Struct. Biol.* **71**, 239–248 (2021).
- Stierl, M. et al. Light modulation of cellular cAMP by a small bacterial photoactivated adenylyl cyclase, bPAC, of the soil bacterium Beggiatoa. J. Biol. Chem. 286, 1181–1188 (2011).
- Kaern, M., Elston, T. C., Blake, W. J. & Collins, J. J. Stochasticity in gene expression: from theories to phenotypes. *Nat. Rev. Genet.* 6, 451–464 (2005).
- 35. Del Vecchio, D., Dy, A. J. & Qian, Y. Control theory meets synthetic biology. J. R. Soc. Interface 13, 20160380 (2016).
- van Roekel, H. W. et al. Programmable chemical reaction networks: emulating regulatory functions in living cells using a bottom-up approach. Chem. Soc. Rev. 44, 7465–7483 (2015).
- 37. Brophy, J. A. & Voigt, C. A. Principles of genetic circuit design. *Nat. Methods* 11, 508–520 (2014).
- 38. Kwon, K. K., Lee, J., Kim, H., Lee, D.-H. & Lee, S.-G. Advancing high-throughput screening systems for synthetic biology and biofoundry. *Curr. Opin. Syst. Biol.* **37**, 100487 (2024).
- 39. Coggan, K. A. & Wolfgang, M. C. Global regulatory pathways and cross-talk control *Pseudomonas aeruginosa* environmental lifestyle and virulence phenotype. *Curr. Issues Mol. Biol.* **14**, 47–70 (2012).
- Gneiting, T., Ševčíková, H. & Percival, D. B. Estimators of fractal dimension: assessing the roughness of time series and spatial data. Stat. Sci. 27, 247–277 (2012).
- 41. Mar, J. C. & Quackenbush, J. Decomposition of gene expression state space trajectories. *PLoS Comput. Biol.* **5**, 1000626 (2009).
- 42. Shannon, C. E. A mathematical theory of communication. *Bell Syst. Tech. J.* **27**, 379–423 (1948).
- 43. Cheong, R., Rhee, A., Wang, C. J., Nemenman, I. & Levchenko, A. Information transduction capacity of noisy biochemical signaling networks. *Science* **334**, 354–358 (2011).
- 44. Nandagopal, N. & Elowitz, M. B. Synthetic biology: integrated gene circuits. Science **333**, 1244–1248 (2011).

- 45. Levine, J. H., Lin, Y. & Elowitz, M. B. Functional roles of pulsing in genetic circuits. *Science* **342**, 1193–1200 (2013).
- Chuang, C.-H. & Lin, C.-L. Synthesizing genetic sequential logic circuit with clock pulse generator. BMC Syst. Biol. 8, 63 (2014).
- Tomazou, M., Barahona, M., Polizzi, K. M. & Stan, G.-B.
 Computational re-design of synthetic genetic oscillators for independent amplitude and frequency modulation. *Cell Syst.* 6, 508–520 (2018).
- Appleton, E., Madsen, C., Roehner, N. & Densmore, D. Design automation in synthetic biology. *Cold Spring Harb. Perspect. Biol.* 9, 023978 (2017).
- Zhang, R. et al. High-throughput, microscopy-based screening and quantification of genetic elements. mLife 2, 450–461 (2023).
- 50. Delvigne, F. & Martinez, J. A. Advances in automated and reactive flow cytometry for synthetic biotechnology. *Curr. Opin. Biotechnol.* **83**, 102974 (2023).
- Foncillas, R. P. et al. Automated yeast cultivation control using a biosensor and flow cytometry. J. Ind. Microbiol. Biotechnol. 51, kuae039 (2024).
- 52. Purvis, J. E. et al. p53 dynamics control cell fate. Science **336**, 1440–1444 (2012).
- Imayoshi, I. et al. Oscillatory control of factors determining multipotency and fate in mouse neural progenitors. Science 342, 1203–1208 (2013).
- 54. Tay, S. et al. Single-cell NF-κB dynamics reveal digital activation and analogue information processing. *Nature* **466**, 267–271 (2010).

- 55. Lu, T. K., Khalil, A. S. & Collins, J. J. Next-generation synthetic gene networks. *Nat. Biotechnol.* **27**, 1139–1150 (2009).
- 56. Eldar, A. & Elowitz, M. B. Functional roles for noise in genetic circuits. *Nature* **467**, 167–173 (2010).

Publisher's note Springer Nature remains neutral with regard to jurisdictional claims in published maps and institutional affiliations.

Open Access This article is licensed under a Creative Commons Attribution-NonCommercial-NoDerivatives 4.0 International License, which permits any non-commercial use, sharing, distribution and reproduction in any medium or format, as long as you give appropriate credit to the original author(s) and the source, provide a link to the Creative Commons licence, and indicate if you modified the licensed material. You do not have permission under this licence to share adapted material derived from this article or parts of it. The images or other third party material in this article are included in the article's Creative Commons licence, unless indicated otherwise in a credit line to the material. If material is not included in the article's Creative Commons licence and your intended use is not permitted by statutory regulation or exceeds the permitted use, you will need to obtain permission directly from the copyright holder. To view a copy of this licence, visit http://creativecommons.org/licenses/by-nc-nd/4.0/.

© The Author(s) 2025

¹State Key Laboratory of Quantitative Synthetic Biology, Shenzhen Institute of Synthetic Biology, Shenzhen Institutes of Advanced Technology, Chinese Academy of Sciences, Shenzhen, China. ²Shenzhen Synthetic Biology Infrastructure, Shenzhen Institute of Synthetic Biology, Shenzhen Institutes of Advanced Technology, Chinese Academy of Sciences, Shenzhen, China. ³Hefei National Research Center for Physical Sciences at the Microscale, Department of Polymer Science and Engineering, University of Science and Technology of China, Hefei, China. ⁴National Science Library (Chengdu), Chinese Academy of Sciences, Chengdu, China. ⁵Department of Information Resources Management, School of Economics and Management, University of Chinese Academy of Sciences, Beijing, China. ⁶These authors contributed equally: Rongrong Zhang, Shengjie Wan. ⊠e-mail: yangs@clas.ac.cn; fan.jin@siat.ac.cn

Methods

Computational model

In this study, we use deterministic mass-action CRN models to simulate the system. The genetic circuit FDCC, comprising ten distinct species and nine chemical reactions (Supplementary Table 1, r1-r9), is at the core of these models. Supplementary Table 2 shows a diagram that provides a more realistic representation of the CRN within a bacterium. The reaction parameters used in this model, drawn from existing literature or our experimental data, are detailed in Supplementary Table 3. In this model, we simplify the processes of transcription and translation of CpdA and Vfr, treating them as constants determined by the bacterial strain. The simulation model further streamlines the transcription and translation of proteins into a single step, and introduces a deactivation stage for bPAC to incorporate the non-instantaneous deactivation of bPAC post-light exposure.

Parameter estimation and fitting procedures

Using an automated detection platform, we systematically measured fluorescence outputs (F_T) under fixed duty cycle conditions (D = 0.3)across various oscillation periods T(100 s, 300 s, 500 s, 900 s, 1,800 s)and 2,400 s), with dark controls (F_{Dark}) and continuous illumination (F_{Light}) serving as reference measurements. Fluorescence quantification used two normalization approaches: for samples containing internal controls, we used the ratio of reporter gene sfGFP fluorescence to internal standard CyOFP fluorescence; for samples without internal standards, we applied OD-normalized reporter fluorescence intensity. Normalized response values $Y = (F_T - F_{Dark})/(F_{Light} - F_{Dark})$ were calculated to generate frequency response curves for each engineered strain. We initially constructed a strain library with varying expression levels of CpdA and Vfr. Preliminary characterization revealed that high CpdA expression led to weak output signals and attenuated frequency response under continuous illumination. To optimize the dynamic performance, we maintained the native promoter upstream of bPAC in the frequency-responsive strains identified during initial screening and finely tuned the expression levels of CpdA and Vfr.

Mathematical modelling revealed that under constant D, the response Y exhibits functional dependence on oscillation period T, hydrolysis rate γ , and dimensionless parameters α and λ . We used two distinct fitting approaches to determine the system parameters from the experimental frequency response data, as detailed in the parameter fitting flowchart (Extended Data Fig. 2).

Fit1 method (multiparameter joint optimization): by fitting the experimentally obtained Y-T curves with γ , α and λ as free parameters and incorporating the parameter–protein concentration relationships detailed in Supplementary Note 9, we derived the concentration values of $[\operatorname{CpdA}]_0$, $[\operatorname{Vfr}]_0$ and $[\operatorname{bPAC}^*]$. Given the relationships $\alpha = k_0[\operatorname{bPAC}^*]/(\gamma K_1)$ and $\lambda = [\operatorname{Vfr}]_0/K_2$, where γ depends on the CpdA and Vfr concentrations through $\gamma = \frac{\gamma_0[\operatorname{CpdA}]_0/K_0}{1+[\operatorname{CpdA}]_0/K_0}(\gamma_0)$ is the hydrolysis rate mediated by CpdA and K_0 is the Michaelis constant), we performed curve fitting using equation (6) from the main text. The characteristic frequency parameter s^* was determined through the relation $s^* = 1/\sqrt{3\alpha^2(1+\lambda)}$.

Fit2 method (composite parameter approach): alternatively, using the more detailed equations (9) and (10) from the main text, we can directly extract the parameters γ and s by fitting the Y-T curves. This method consolidates α and λ into the composite parameter s, enabling more robust parameter determination through reduced optimization complexity.

Our systematic approach involved engineering 65 distinct FDCC variants by systematically varying promoters and RBS sequences controlling CpdA and Vfr expressions. Since λ scales directly with Vfr concentration ($\lambda = [Vfr]_0/K_2$), we obtained strains with varying γ , α and λ values. Through systematic characterization of the engineered strains' frequency response profiles, we successfully identified strains exhibiting measurable high-frequency responses.

All the fitting procedures incorporated physiologically realistic constraints based on established protein concentration ranges: $\gamma \in [0.001, 0.055] \, \text{s}^{-1}$ (cAMP hydrolysis rate), $\lambda \in [10, 500]$ (relative transcription factor abundance) and $s^{*} \in [0.005, 1]$ (normalized threshold), corresponding to intracellular protein concentrations of $0.1-5 \, \mu \text{M}$ as validated through fluorescence microscopy calibration. The detailed data fitting methodology, including all relevant parameters used in Fig. 3, is provided in Extended Data Fig. 2 and Supplementary Note 14.

Cultivation of bacterial strains

In this study, genetically engineered P. aeruginosa strains were cultured at 37 °C. Unless otherwise specified, biological replicates in this study refer to the separate cultivation of individual clones. Strains carrying the bPAC fragment were protected from light throughout the cultivation process. The detailed cultivation protocol involved streaking strains stored at -80 °C on LB agar plates shielded from light with foil. After overnight incubation for resuscitation, single colonies were selected and transferred to the FAB culture medium 57 containing 30 mM of glutamate and 1 μ M of FeCl $_3$. Cultures were agitated at 220 rpm until OD $_{600}$ reached approximately 0.5. Antibiotic concentrations used during cultivation were 30 μ g ml $^{-1}$ of gentamicin, 100 μ g ml $^{-1}$ of tetracycline and 150 μ g ml $^{-1}$ of carbenicillin.

Construction of bacterial strains

All plasmids, strains and promoter sequences are listed in Supplementary Tables 6-8. Unless otherwise specified, the knockout of all genes and the seamless insertion of gene fragments into the genome in this study were accomplished using CRISPR technology. The construction of relevant plasmids was carried out using Gibson assembly. Supplementary Notes 10 and 11 provide additional details on the construction strategies for more bacterial strains and plasmids. The chassis strain FAC01:PAO1-ΔpslBCDΔpelAΔexoSΔexoTΔcyaAΔcyaB was constructed by the successive knockout of six gene clusters. The experimental procedure was refined based on existing literature⁵⁸, with the deletion of the cyaA gene as an example. The specific experimental procedure is as follows. (1) Construct a plasmid PCRISPR-cyaA containing the gRNA and homologous recombination segment. (2) Transform the plasmid PCASPA containing Cas9 into the PAO1 strain, electroporate the plasmid PCRISPR-cyaA, and plate on a double-resistant plate containing tetracycline and carbenicillin. (3) PCR confirms the successful knockout of the target gene cvaA in the resulting colonies. Pick colonies and culture overnight on LB agar plates without sodium chloride at 15% (wt) surcose to loss plasmids. Sequence verification will confirm the PAO1-\(\Delta\)cyaA strain. Subsequent knockouts of genes like \(pslBCD\), pelA, exoS, exoT and cyaB can be performed in a similar manner in the PAO1-ΔcyaA strain. Subsequently, through the integration of the PA1/O4/O3-bPAC fragment into the FAC01 genome utilizing the CTX transposon insertion system, the engineered strain FAC03 was successfully generated.

In the wild-type PAO1 strain, the expression of the vfr and cpdA genes is regulated by cAMP. To eliminate this specific influence, we used CRISPR technology to seamlessly replace the promoters of these genes with constitutive promoters in the FAC03 bacterial genome (Supplementary Note 11). The selectable RBS options encompass B0034-RBS0 46-RBS004-RBS017-RBS021 (ref. 59), whereas the available promoters include J23106-J23115-J23110-J23100-J23102. Through diverse combinations, a total of 65 strains were systematically engineered.

To assess the intracellular expression levels of cAMP, we constructed a plasmid designated as Plac-sfGFP-TOT1-J23102-CyOFP-pJN1 05 and subsequently electroporated it into various chassis cells. Unless otherwise specified, all strains referenced in the main figures contain this plasmid. The constitutively expressed CyOFP fluorescent protein serves as an internal standard for normalizing bacterial growth differences. The change in intracellular cAMP concentration is calculated by comparing the ratio of sfGFP to CyOFP.

Automated experiment

The automation island depicted in Fig. 3a serves as a consolidated area in which automation instruments, equipment and control modules catering to specific experimental functions are harmoniously integrated. Components include robotic arms, microplate reader (Tecan, Spark), incubator (LiCONiC, STX44-ICBT), liquid handler (Tecan, Fluent 780), plate hotel (LiCONiC, LPX220), microplate washer (Tecan, HydroFlex) and a self-developed steering platform. The intelligent control system comprises various modules such as process editing, task scheduling, data analysis, equipment management and so on. For instance, the task scheduling system can precisely coordinate equipment operations to achieve automated workflow, and the data analysis system can collect and analyse experimental data in real time.

Supplementary Video 1 presents a comprehensive demonstration of an automated experimental workflow. The automated platform allows for the concurrent parallel execution of multiple tasks. Using our self-developed light control device OPCU, we can program the input of light signal intensity *I*, period *T* and duty cycle *D*. Subsequently, we dispense the bacterial solution into 96-well black plates (LABSELECT, 11514), install the plate into the OPCU and place it in the WareHotels of the automation island. Then, we start the experiment to achieve the continuous dilution of bacteria and data collection. The procedure and script for the automated experiment are detailed in Supplementary Fig. 4 and Supplementary Note 12.

Bacterial image acquisition

After the completion of the automated experiment, following the method previously described, the rapid high-throughput acquisition of microscopic images of a single bacterium in a 96-well plate is conducted. The experimental steps are outlined as follows. First, we prepare a 1% agar plate of FAB medium in a 96-well format, with the composition of the medium identical to that used in the automated experiment. Next, we pipette 6 µl of the bacterial suspension onto the corresponding wells of the agar plate. Finally, we compress the bacterial suspension to a thickness of 0.17 mm on a specialized microscope slide. Each well corresponds to a different bacterial strain, and the OPCU is used to set independent illumination conditions for each well. We use a fluorescence microscope (IX-71, Olympus) equipped with a ×100 oil objective to capture four fields of view for each well, with approximately 500 bacteria per field, acquiring fluorescent images. Fluorescent images of sfGFP, CyOFP and mScarlet were acquired by two Zyla 4.2 scientific complementary metal-oxidesemiconductor cameras. The fluorescence of sfGFP, CvOFP and mScarlet was excited using a solid-state light source (Lumencor SPECTRAX).

Reporting summary

Further information on research design is available in the Nature Portfolio Reporting Summary linked to this article.

Data availability

The data supporting the findings of this study are available within the Article and its Supplementary Information. Source data are provided with this paper.

References

- Xiong, J. et al. Quantifying second-messenger information transmission in bacteria. Nat. Phys. 21, 1009–1018 (2025).
- 58. Chen, W. et al. CRISPR/Cas9-based genome editing in Pseudomonas aeruginosa and cytidine deaminase-mediated base editing in Pseudomonas species. iScience 6, 222–231 (2018).
- 59. Fu, S. et al. Programming the lifestyles of engineered bacteria for cancer therapy. *Natl Sci. Rev.* **10**, nwadO31 (2023).

Acknowledgements

We specially thank A. Xia for guidance and assistance with microscope usage, L. Wang for developing the experimental setup, and Shenzhen

Infrastructure for Synthetic Biology for providing the experimental platform and technical support for the automated characterization in this work. This work was supported by the National Key Research and Development Program of China (grant number 2020YFA0906900, F.J.), the Strategic Priority Research Program of the Chinese Academy of Sciences (grant number XDB0480000, F.J.), the National Natural Science Foundation of China (grant number 32471489, F.J.; grant number 32101177, Y.H.; grant number 32101002, Y.L.), Shenzhen Engineering Research Center of Therapeutic Synthetic Microbes (grant number XMHT20220104015, F.J.) and the Innovation Foundation of National Science Library (Chengdu) (grant number E3Z0000903, S.Y.).

Author contributions

Project conceptualization and supervision: F.J. led the conceptual development; F.J. and S.Y. provided project supervision. Theoretical framework development: F.J. developed the foundational framework including Figs. 1a and 2a; F.J., S.Y. and J.X. derived the core theoretical equations (1)-(10); J.X. established the threshold theory, characterized the threshold-duty cycle relationships, and extended analysis to FM and n-dimensional spaces; S.Y. and S.W. conducted the theoretical validation through simulations. FAC multigene control system: F.J. provided the conceptual framework; R.Z. designed the experimental approaches; S.W. performed the simulation validation. Automated experimental platform: R.Z. developed the experimental processes; Y.L. integrated the hardware and software systems. CRN analysis: F.J., S.Y., S.W., J.X. and L.N. collaborated on the CRN construction and analysis. Computational studies: S.W. and S.Y. performed the simulations. Gene circuit implementation: S.Y. developed the design framework and simulations; R.Z. performed the experimental characterization; S.W. conducted the parameter fitting. Molecular biology: R.Z., Y.H., S.Y., B.L. and M.L. performed the molecular cloning and primer design. Promoter library development: S.Y., R.Z. and B.L. conducted the screening and characterization. Automated experimental development: R.Z. and Y.L. optimized the automated workflows. Data analysis: S.Y., S.W. and L.N. developed the analysis pipelines; S.W., R.Z. and S.Y. analysed the experimental data; S.W., R.Z. and J.X. performed the model fitting. Strain development: R.Z., B.L. and M.L. maintained the bacterial cultures. Protocol development: R.Z. and S.Y. established and validated the experimental procedures. Paper preparation: S.Y. wrote the main text and contributed the figures: R.Z., S.W. and J.X. contributed the figures, video and Supplementary Information. Paper review: F.J., S.Y., R.Z., S.W. and J.X. revised and reviewed the paper.

Competing interests

The authors declare no competing interests.

Additional information

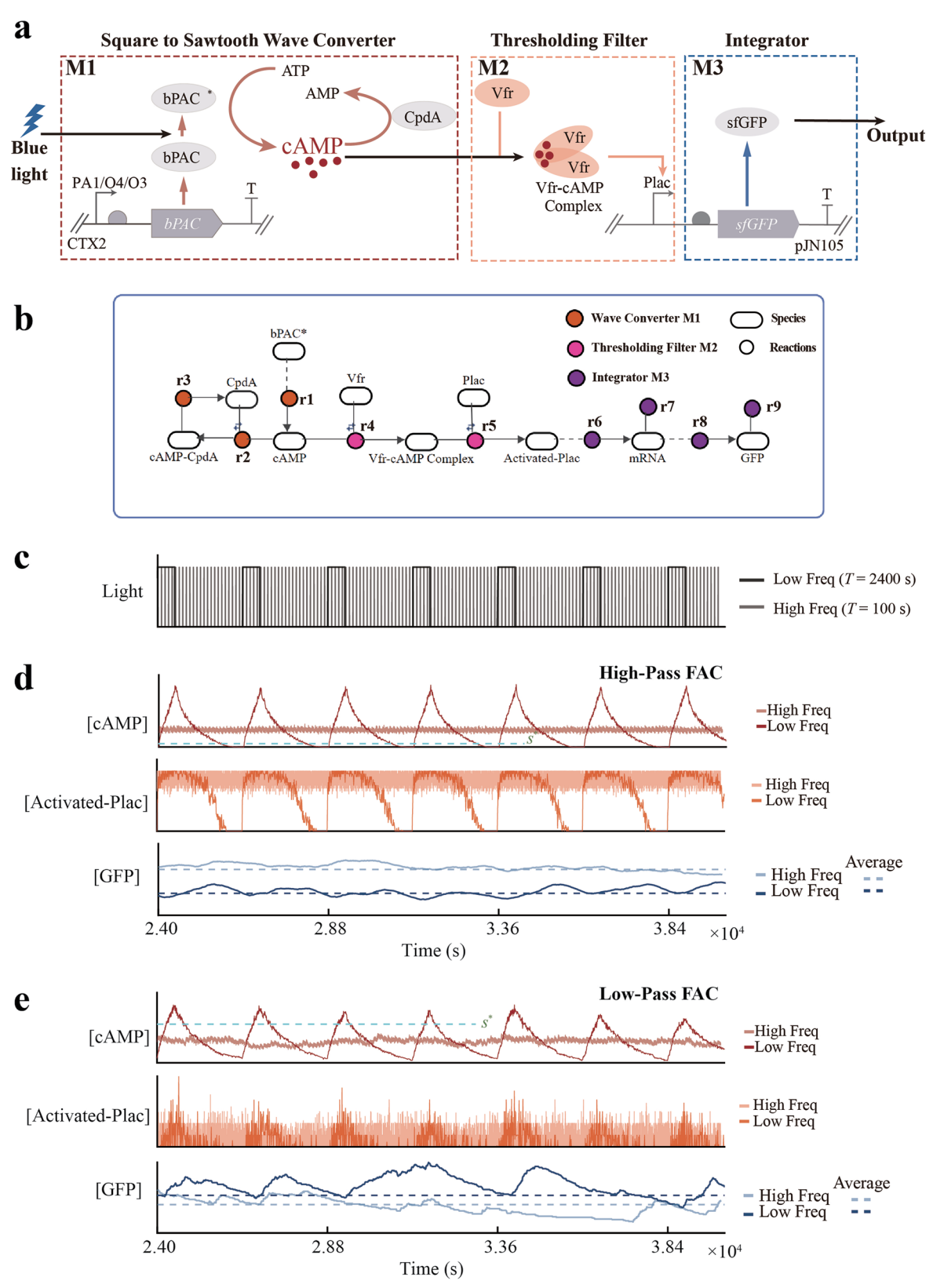
Extended data is available for this paper at https://doi.org/10.1038/s41567-025-03030-4.

Supplementary information The online version contains supplementary material available at https://doi.org/10.1038/s41567-025-03030-4.

Correspondence and requests for materials should be addressed to Shuai Yang or Fan Jin.

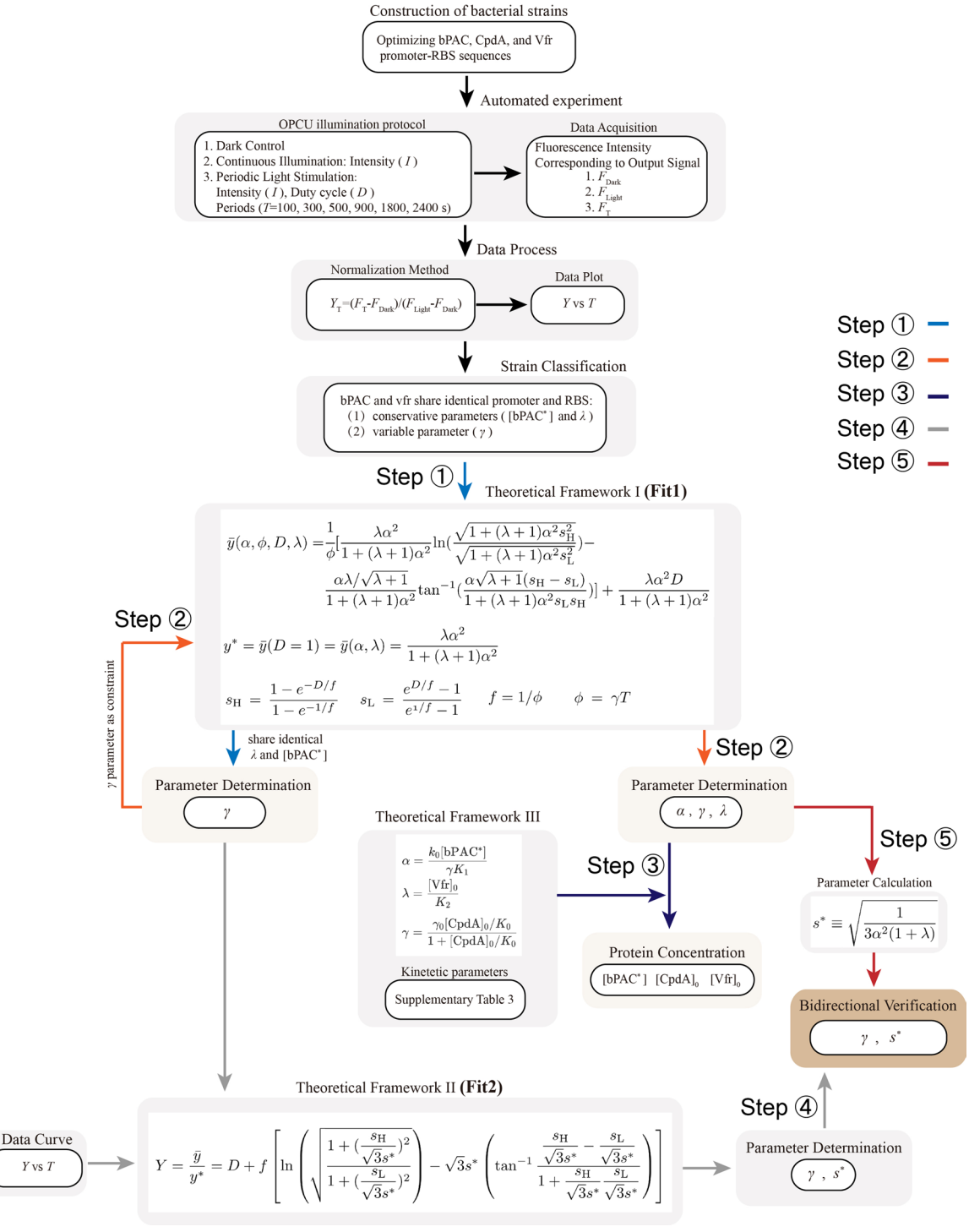
Peer review information *Nature Physics* thanks Lei Wei and the other, anonymous, reviewer(s) for their contribution to the peer review of this work.

Reprints and permissions information is available at www.nature.com/reprints.



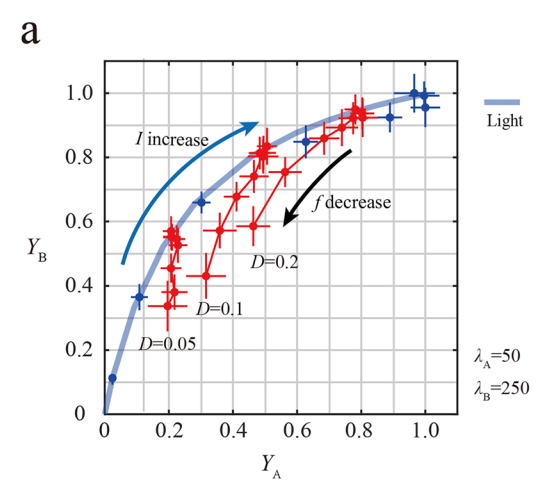
Extended Data Fig. 1 | The Chemical Reaction Network (CRN) model and simulation results corresponding to the FDCC. a, Molecular implementation of the Frequency-Decoding cAMP Circuit (FDCC). Optogenetic circuit design incorporating light-activated bPAC and CpdA phosphodiesterase (M1), cAMP-dependent Vfr transcription factor binding (M2), and protein expression machinery (M3). b, The simplified CRN model utilized for simulation. The ellipses represent species in the FDCC, while the circles represent reactions. The orange, pink, and purple circles correspond to the kinetic reactions within

modules Wave Converter (M1), Thresholding Filter (M2), and Integrator (M3), respectively. \mathbf{c} , Input signals to the simulation: a high-frequency input of $1/100~\text{s}^{-1}$ and a low-frequency input of $1/2400~\text{s}^{-1}$. \mathbf{d} , Simulation output from the high-pass configuration after reaching equilibrium. Parameter settings: [bPAC'] = $0.1~\mu$ M (equivalent to 50 molecules under the conversion 2 nM = 1 molecule), [CpdA] $_0$ = $0.15~\mu$ M, [Vfr] $_0$ = $0.1~\mu$ M, and [Plac] $_0$ = 40~nM. \mathbf{e} , Simulation output from the low-pass configuration after reaching equilibrium. Parameter settings: [bPAC'] = $5.0~\mu$ M, [CpdA] $_0$ = $2.0~\mu$ M, [Vfr] $_0$ = $2.0~\mu$ M, and [Plac] $_0$ = 40~nM.

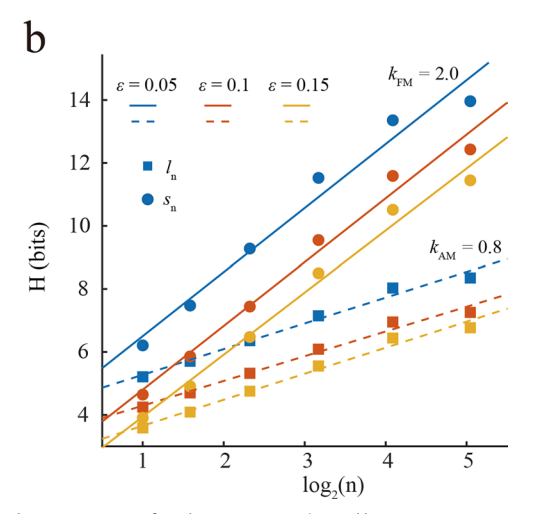


Extended Data Fig. 2 | Data processing and formula fitting workflow diagram. Systematic fitting process for the experimental strains shown in Fig. 3f. The engineered strains constructed with fixed initial bPAC concentrations at three different Vfr expression levels, with fine-tuned CpdA expression. Experimental data collection was performed using an automated platform, recording the fluorescence intensity (Y) of output proteins at different input frequencies, which were then normalized to generate frequency-response curves (Yvs T). The data analysis adopted a hierarchical fitting strategy: First, strains were classified into three groups based on Vfr expression levels, assuming that strains within the same group shared identical λ and [bAPC]. Global fitting

(Fit1) was performed to obtain strain-specific γ values and shared parameters (Step-1). Subsequently, precise fitting optimization (Step-2) was conducted by constraining the range of γ values. Based on the correlation model established in Supplementary Note 8.4, the fitted parameters were converted to protein concentrations (Step-3). Using the Fit2 model (Step-4), or by calculation based on the α and λ parameters obtained from Fit1 (Step-5) to determain parameter s. It should be noted that the fitting methods for other independent strain datasets followed essentially the same procedure with only minor differences, as detailed in Supplementary Note 14.



Extended Data Fig. 3 | Quantitative analysis of noise characteristics and information capacity in optogenetic gene circuits. a, Obtained through MATLAB SimBiology stochastic simulations. For the continuous illumination group (blue), varying input light intensities (corresponding to initial bPAC concentrations in the CRN) were applied. The steady-state means of both protein expressions at maximum light intensity served as normalization standards. Data are presented as mean values with error bars representing standard deviation (s.d.) obtained from stochastic simulations. The noise values (error-bar) were obtained from normal distribution fits of steady-state data distributions, normalized by their respective protein expression means. For duty cycle data,



light intensity was fixed at maximum (initial bPAC concentration in CRN set to maximum). Connected data points share identical duty cycles, with three groups having D=0.05, 0.1, and 0.2 respectively, while periods were varied (T=100,200,400,800,1600,2400,3600,5400 seconds). **b**, For different numbers of regulatory genes (n), we calculated the number of states in amplitude modulation only (AM) mode and in combined amplitude and frequency modulation (FM) mode by sampling parameters α,λ,D , and f, with λ taken from a geometric sequence with a common ratio of 2 starting at 50 (that is, λ = 50,100, 200,400...). The information entropy H was then computed. The curve of H versus $\log_2[n]$ was plotted to determine the slope value.

Extended Data Table 1 | Definitions of non-dimensional symbols and abbreviations in this study

Symbols

Physical Significance

- \bar{y} Steady-state average non-dimensional GFP concentration over one period, defined as $\bar{y}=f\int_0^{1/f}\psi(\tau)\ \mathrm{d}\tau$, represents the output signal amplitude of the Frequency-Amplitude Control (FAC) system.
- y^* Steady-state average GFP concentration over one constant light period, defined as $y^* = \bar{y}(D = 1)$.
- Y Non-dimensional representation of protein concentration, defined as $Y = \frac{\bar{y}}{y^*}$. The normalized high-frequency output $Y_{\rm HF}$ (theoretical cutoff: $10^{-1}~{\rm s}^{-1}$) corresponds experimentally to measurements at 100 seconds, and the normalized low-frequency output $Y_{\rm LF}$ (theoretical cutoff: $10^{-5}~{\rm s}^{-1}$) corresponds experimentally to measurements at 2400 seconds.
- $G \qquad \text{Non-dimensional representation of frequency influence on the protein output, defined as: } G = f \left[\ln(\sqrt{\frac{1 + (s_{\rm H}/\sqrt{3}s^*)^2}{1 + (s_{\rm L}/\sqrt{3}s^*)^2}}) \sqrt{3}s^*(\tan^{-1}(\frac{\sqrt{3}s^*(s_{\rm H} s_{\rm L})}{(\sqrt{3}s^*)^2 + s_{\rm H}s_{\rm L}})) \right]$
- ϵ The discretization parameter, represents the resolution interval between distinguishable output states when calculating the number of gene expression states.
- α Parameter representing light intensity, defined as $\alpha = \frac{k}{\gamma K_1} = \frac{k_0 [\text{bPAC}^*]}{\gamma K_1}$.
- λ Non-dimensional parameter representing the relative abundance of transcription factor Vfr, defined as $\lambda = \frac{[\mathrm{Vfr}]_0}{K_2}$.
- ψ Fraction of activated promoters, calculated as: $\psi = \frac{1}{1 + \frac{1}{\lambda}(1 + \frac{1}{\alpha^2 s^2})}$.
- The non-dimensional representation of cAMP concentration, defined as $s = x/(\frac{k}{\gamma})$, where x represents concentration of cAMP, and $\frac{k}{\gamma}$ represents the theoretical maximum concentration of cAMP.
- s^* Threshold of M2 filter, representing the non-dimensional concentration of cAMP, defined as $s^* = s(\psi'' = 0), \ s^* = \sqrt{\frac{1}{3\alpha^2(1+\lambda)}}.$
- s_H, s_L Highest and lowest non-dimensional concentrations of cAMP in one period.
 - τ Non-dimensional time, defined as $\tau = \gamma t$.
 - f Non-dimensional frequency of the period, calculated as $f = \frac{1}{\phi} = \frac{1}{\gamma T}$, where T represents the duration of the light period.
- Duty cycle (D) is the fraction of one period in which light is active, defined as $D = \frac{PW}{T}$, where PW is the active time of the light.

$\textbf{Extended Data Table 2} \ | \ \textbf{Definitions of symbols and abbreviations with physical units in this study}$

Symbols	Unit	Physical Significance
Н	bits	The information entropy, where p_i represents the probability of the system occupying
		state p_i . $H_{\rm AM}$ represents the information entropy calculated solely from amplitude
		modulation. H_{FM} denotes the information entropy computed from both amplitude
		modulation and frequency modulation.
γ	s^{-1}	The apparent hydrolysis rate of cAMP; $\gamma = \frac{\gamma_0 [\text{CpdA}]_0 / K_0}{1 + [\text{CpdA}]_0 / K_0}$
K_0	μM	The microscopic dissociation constant between cAMP and the phosphodiesterase
		CpdA, represents the affinity of the interaction, with the concentration of cAMP
		being the ligand concentration required to achieve half-maximal binding of CpdA.
K_1	μM	The microscopic dissociation constant between cAMP and the transcription factor
		Vfr, represents the affinity of the interaction, with the concentration of cAMP being
		the ligand concentration required to achieve half-maximal binding of Vfr.
K_2	μM	The microscopic dissociation constant for the Vfr-cAMP complex binding to regu-
		latory promoters, reflects the affinity of the complex for these promoters, with the
		concentration of the Vfr-cAMP complex being the ligand concentration required to
		achieve half-maximal binding of the promoters.
$[bPAC^*]$	μM	The concentration of activated state bPAC (bPAC*).
$[\mathrm{Vfr}]_0$	$\mu \mathrm{M}$	The initial concentration of Vfr is primarily determined by the promoter and RBS
		(ribosome binding site) upstream of the gene.
$[\mathrm{Cpd} A]_0$	μM	The initial concentration of CpdA is primarily determined by the promoter and RBS $$
		(ribosome binding site) upstream of the gene.
T_{c1}	\mathbf{S}	The characteristic time of the Wave Converter (M1) ranges from 10^0 to 10^1 seconds.
T_{c2}	\mathbf{S}	The characteristic time of the Thresholding Filter (M2) ranges from 10^{-2} to 100
		seconds.
T_{c3}	\mathbf{S}	The characteristic time of the Integrator (M3) ranges from 10^3 to 10^4 seconds.
T_{c1}	S	The characteristic time of the Wave Converter (M1), ranges from 10^0 to 10^1 seconds.
T_{c2}	\mathbf{S}	The characteristic time of the Thresholding Filter (M2), ranges from 10^{-2} to 100
		seconds.
T_{c3}	S	The characteristic time of the Integrator (M3), ranges from 10^3 to 10^4 seconds.

$\textbf{Extended Data Table 3} \,|\, \textbf{The effect of experimental control parameters on the characteristics of FAC} \,$

Category	Tunable Parameters	Description	Affected Parameters	Corresponding Relationship
	I	Light intensity	α, s^*	$\alpha = \frac{k_0[\text{bPAC}^*]}{\gamma K_1}, \ s^* = \sqrt{\frac{1}{3\alpha^2(1+\lambda)}}$ $f = \frac{1}{\gamma T}$
Signal input parameters	T	Period of square-wave signal	f	$f = \frac{1}{\gamma T}$
	D	Duty cycle of square-wave signal	$D,s_{ m H},s_{ m L}$	$s_{\rm H} = \frac{1 - e^{-\phi D}}{1 - e^{-\phi}}, \ s_{\rm L} = \frac{e^{\phi D} - 1}{e^{\phi} - 1}$
	$[bPAC]_0$	Initial bPAC concentration	α, s^*	$[bPAC^*] \propto [bPAC]_0$
System parameters	$[Vfr]_0$	Initial Vfr concentration	λ,s^*	$\lambda = rac{[ext{Vfr}]_0}{K_2}$
in gene circuit	$[CpdA]_0$	Initial CpdA concentration	γ, α, s^*	$\gamma = \frac{\gamma_0[\text{CpdA}]_0/K_0}{1 + [\text{CpdA}]_0/K_0}$

nature portfolio

Corresponding author(s):	Fan Jin
Last updated by author(s):	Mar 20, 2025

Reporting Summary

Nature Portfolio wishes to improve the reproducibility of the work that we publish. This form provides structure for consistency and transparency in reporting. For further information on Nature Portfolio policies, see our <u>Editorial Policies</u> and the <u>Editorial Policy Checklist</u>.

For all statistical analyses, confirm that the following items are present in the figure legend, table legend, main text, or Methods section.

_					
8	۲a	t۱	ict	۲i	CS
$\boldsymbol{\mathcal{I}}$	u	u		u	-

n/a	Confirmed	
	The exact	sample size (n) for each experimental group/condition, given as a discrete number and unit of measurement
\boxtimes	A stateme	ent on whether measurements were taken from distinct samples or whether the same sample was measured repeatedly
\boxtimes		tical test(s) used AND whether they are one- or two-sided on tests should be described solely by name; describe more complex techniques in the Methods section.
\boxtimes	A descript	ion of all covariates tested
\boxtimes	A descript	ion of any assumptions or corrections, such as tests of normality and adjustment for multiple comparisons
	A full desc	cription of the statistical parameters including central tendency (e.g. means) or other basic estimates (e.g. regression coefficient) tion (e.g. standard deviation) or associated estimates of uncertainty (e.g. confidence intervals)
\boxtimes		pothesis testing, the test statistic (e.g. F , t , r) with confidence intervals, effect sizes, degrees of freedom and P value noted as as exact values whenever suitable.
\boxtimes	For Bayes	ian analysis, information on the choice of priors and Markov chain Monte Carlo settings
\boxtimes	For hierar	chical and complex designs, identification of the appropriate level for tests and full reporting of outcomes
\boxtimes	Estimates	of effect sizes (e.g. Cohen's d , Pearson's r), indicating how they were calculated
		Our web collection on <u>statistics for biologists</u> contains articles on many of the points above.
Sof	ftware an	d code
Polic	cy information	about <u>availability of computer code</u>
Da	ata collection	Data acquisition and analysis were performed using an Olympus IX81 inverted fluorescence microscope and MATLAB R2021a software suite. Chemical reaction networks were constructed using the SimBiology package (version 6.2).

Data

Data analysis

Policy information about availability of data

All manuscripts must include a <u>data availability statement</u>. This statement should provide the following information, where applicable:

For manuscripts utilizing custom algorithms or software that are central to the research but not yet described in published literature, software must be made available to editors and reviewers. We strongly encourage code deposition in a community repository (e.g. GitHub). See the Nature Portfolio guidelines for submitting code & software for further information.

- Accession codes, unique identifiers, or web links for publicly available datasets

MATLAB (R2021a), SimBiology (version 6.2)

- A description of any restrictions on data availability
- For clinical datasets or third party data, please ensure that the statement adheres to our <u>policy</u>

The data availability statement is included in our paper and raw data are provided in source data files.

Research involving human participants, their data, or biological material

and sexual orientation		thicity and racism.
Reporting on sex ar	nd gender	N/A
Reporting on race, other socially relev- groupings	, .	N/A
Population charact	eristics	N/A
Recruitment		N/A
Ethics oversight		N/A
Note that full information	on on the appro	oval of the study protocol must also be provided in the manuscript.
Field-spec	cific re	porting
Please select the one	below that is	the best fit for your research. If you are not sure, read the appropriate sections before making your selection.
X Life sciences	Ве	ehavioural & social sciences
or a reference copy of the	e document with a	ill sections, see <u>nature.com/documents/nr-reporting-summary-flat.pdf</u>
Life sciend	ces stu	ıdy design
All studies must discl	ose on these p	points even when the disclosure is negative.
F C 8 6 C	orecisely tuned construction, we genetic circuit b establishing a re observations. Th	vely assess how protein expression levels influence the frequency signal decoding performance of the genetic circuit, we protein expression by modulating the ribosome binding site (RBS) strength upstream of the target gene. During strain a designed RBS variants spanning two orders of magnitude in strength, allowing systematic investigation of factors governing ehavior. To define the input frequency range, we coupled intracellular cAMP degradation kinetics with circuit parameters, duced frequency range over one order of magnitude—a regime where the analytical model precisely matches experimental he integration of experimental data with theoretical modeling confirms that the engineered bacterial population and tup provide comprehensive parameter coverage, thereby ensuring robust conclusions.
е г іі	experimental da microplate read ntroduce signifi	f how the constructed bacterial strains decode frequency signals, we established a priori exclusion criteria for automated ita, specifically excluding data points where the bacterial response frequency signals fell below the detection threshold of the er's fluorescence assay. This exclusion was necessitated by the fact that bacterial strains exhibiting weak output signals would cant errors, thereby biasing the relationship between the frequency input signal and the output signal. Therefore, these data unded to ensure robust analysis of the frequency signal decoding process in the genetic circuit.
s		s were independently performed multiple times, with each replication involving fresh bacterial cultures, frequency automated experiment. All experimental findings were reproducible across these independent replicates, demonstrating the results.
Randomization N	Not relevant to	this study. We did not test effects of interventions or perform hypothesis tests.

Reporting for specific materials, systems and methods

both produced and analysed the data.

Blinding

We require information from authors about some types of materials, experimental systems and methods used in many studies. Here, indicate whether each material, system or method listed is relevant to your study. If you are not sure if a list item applies to your research, read the appropriate section before selecting a response.

Researchers were not blinded to group allocation during data collection and analysis. Blinding was not possible as the same researchers

Materials & experimental systems	Methods	
n/a Involved in the study	n/a Involved in the study	
Antibodies	ChIP-seq	
Eukaryotic cell lines	Flow cytometry	
Palaeontology and archaeology	MRI-based neuroimaging	
Animals and other organisms		
Clinical data		
Dual use research of concern		
Plants		

Plants

Seed stocks

Report on the source of all seed stocks or other plant material used. If applicable, state the seed stock centre and catalogue number. If plant specimens were collected from the field, describe the collection location, date and sampling procedures.

Novel plant genotypes

Describe the methods by which all novel plant genotypes were produced. This includes those generated by transgenic approaches, gene editing, chemical/radiation-based mutagenesis and hybridization. For transgenic lines, describe the transformation method, the number of independent lines analyzed and the generation upon which experiments were performed. For gene-edited lines, describe the editor used, the endogenous sequence targeted for editing, the targeting guide RNA sequence (if applicable) and how the editor was applied.

Authentication

was applied.

Describe any authentication procedures for each seed stock used or novel genotype generated. Describe any experiments used to assess the effect of a mutation and, where applicable, how potential secondary effects (e.g. second site T-DNA insertions, mosiacism, off-target gene editing) were examined.